



## 저작자표시-비영리-변경금지 2.0 대한민국

이용자는 아래의 조건을 따르는 경우에 한하여 자유롭게

- 이 저작물을 복제, 배포, 전송, 전시, 공연 및 방송할 수 있습니다.

다음과 같은 조건을 따라야 합니다:



저작자표시. 귀하는 원저작자를 표시하여야 합니다.



비영리. 귀하는 이 저작물을 영리 목적으로 이용할 수 없습니다.



변경금지. 귀하는 이 저작물을 개작, 변형 또는 가공할 수 없습니다.

- 귀하는, 이 저작물의 재이용이나 배포의 경우, 이 저작물에 적용된 이용허락조건을 명확하게 나타내어야 합니다.
- 저작권자로부터 별도의 허가를 받으면 이러한 조건들은 적용되지 않습니다.

저작권법에 따른 이용자의 권리는 위의 내용에 의하여 영향을 받지 않습니다.

이것은 [이용허락규약\(Legal Code\)](#)을 이해하기 쉽게 요약한 것입니다.

[Disclaimer](#)

공학석사 학위논문

**Facile Preparation of N-doped  
and Interconnected Porous  
Carbon Nanosheets for High-  
performance Supercapacitors  
with Redox Additives in Aqueous  
Electrolyte**

질소 도핑된 상호연결 구조의 다공성 탄소  
나노시트의 간편한 제작과 산화환원 첨가제가  
포함된 수용액 기반의 슈퍼커패시터에의 응용

2020년 8월

서울대학교 융합과학기술대학원

융합과학부 나노융합전공

김 덕 환

# **Facile Preparation of N-doped and Interconnected Porous Carbon Nanosheets for High- performance Supercapacitors with Redox Additives in Aqueous Electrolyte**

Deokhwan Kim

Program in Nano Science and Technology

Graduate School of Convergence Science & Technology

Seoul National University

## Abstract

N-doped porous carbon nanosheets have garnered research attention owing to their effective structure for fast ion diffusion and pseudocapacitive properties in supercapacitors. Herein, a facile method to incorporate nitrogen into interconnected porous carbon nanosheets with relatively high doping efficiency is proposed by inducing melamine condensation through appropriate dwell time. The as-prepared N-doped porous carbon material was studied as an electrode for the electrochemical double-layer capacitor. The carbon material delivered a specific capacitance of  $350 \text{ F g}^{-1}$  at a current density of  $1 \text{ A g}^{-1}$  in a three-electrode system. Furthermore, a symmetric supercapacitor device was fabricated using the N-doped interconnected carbon nanosheets with redox additives in aqueous electrolyte. Based on the redox reaction of the electrodes and electrolytes, the specific capacitance was measured  $468 \text{ F g}^{-1}$  at a current density of  $1 \text{ A g}^{-1}$  and  $233 \text{ F g}^{-1}$  at a relatively high current density of  $20 \text{ A g}^{-1}$ . This research provided an efficient method for nitrogen-doping into interconnected porous carbon nanosheets using melamine and showed potential of carbon electrode material for high-

performance supercapacitor applications with redox additives in aqueous electrolyte.

**Keywords:** Porous carbon nanosheets, Supercapacitors, N-doping, Redox additive electrolytes

**Student Number:** 2018-24374

# Contents

<b>1. Introduction .....</b>	<b>12</b>
1.1. Supercapacitor .....	12
1.2. Porous carbon nanosheets .....	12
1.3. Nitrogen doping .....	13
1.4. Redox additive in aqueous electrolyte .....	14
1.5. Objective .....	15
 <b>2. Experimental Section.....</b>	<b>16</b>
2.1. Preparation of PCN .....	16
2.2. Preparation of N-doped PCN .....	16
2.3. Material characterizations .....	17
2.4. Electrochemical characterizations .....	18
 <b>3. Results and Discussion .....</b>	<b>20</b>
3.1. Material analysis .....	20
3.2. Electrochemical analysis.....	37

<b>4. Conclusions .....</b>	<b>47</b>
-----------------------------	-----------

<b>References .....</b>	<b>48</b>
-------------------------	-----------

<b>국문 초록 (Abstract in Korean) .....</b>	<b>56</b>
---	-----------

## List of Figures

<b>Figure 1.</b>	a) Synthesis process of NPCN. b) Heat treatment with the dwell time for condensation of melamine. c) Condensation process from melamine to melem.....	21
<b>Figure 2.</b>	FTIR spectra of NPCN-14D@580 and NPCN-14@580... ..	23
<b>Figure 3.</b>	SEM images of the prepared samples of a, b) PCN, c, d) NPCN-11D, e, f) NPCN-14D g, h) NPCN-14 with low and relatively high-magnification.. ..	25
<b>Figure 4.</b>	a) HR-TEM image and b) EDS mapping of NPCN-14D..	27
<b>Figure 5.</b>	a) Nitrogen adsorption/desorption isotherm curves and b) Pore size distributions of PCN and NPCN-14D.. ..	29
<b>Figure 6.</b>	a) Raman spectra of NPCNs and PCN. ....	32



**Figure 7.** a) XPS survey spectra of NPCNs and PCN. b) Nitrogen configurations of NPCNs.. ..... 35

**Figure 8.** Electrochemical performances of PNC and NPCNs in the three-electrode system with 6M KOH electrolyte. a) CV curves at a scan rate of  $50 \text{ mV s}^{-1}$ , b) Specific capacitances at various current densities from 1 to  $20 \text{ A g}^{-1}$  of PCN, NPCN-11D, and NPCN-14D. c) CV curves at various scan rates from 10 to  $500 \text{ mV s}^{-1}$ , d) GCD curves at various current densities from 1 to  $20 \text{ A g}^{-1}$  of NPCN-14D..... 39

**Figure 9.** a) A color change of the dopamine solution resulting from the electrochemical polymerization and b) DLS measurement of IME.. ..... 41

**Figure 10.** Electrochemical performances of NPCN-14D in the symmetric supercapacitors with IME. a) CV curves at various scan rates from 25 to  $1000 \text{ mV s}^{-1}$ . b) GCD curves and c) Specific capacitances at various current densities from 5 to  $100 \text{ A g}^{-1}$ . d) Nyquist plot... ..... 44

<b>Figure 11.</b> a) Cycle performance at $20 \text{ A g}^{-1}$ and b) Ragone plots of the symmetric supercapacitor.. . . .	46
--	----

## List of Tables

<b>Table 1.</b>	Structural properties of PCN and NPCN-14D obtained from nitrogen adsorption/desorption analysis... ..	30
<b>Table 2.</b>	Chemical compositions of PCN and NPCNs obtained from XPS and EA.....	36

# **1. Introduction**

## **1.1. Supercapacitors**

Supercapacitors are receiving considerable attention as next-generation energy-storage devices because of their high power characteristics and long lifespan [1, 2]. There are two kinds of supercapacitors based on the charge storage mechanism: electrochemical double-layer capacitors (EDLCs) and pseudo-capacitors [3, 4]. The EDLCs store the charge through adsorption/desorption of electrolyte ions to the electrode surface, while in pseudo-capacitors, the charge is stored by a reversible faradic reaction. Carbonaceous materials have been mainly used as electrode materials in EDLCs owing to their high specific surface area, good electrical conductivity, and chemical stability [5-9].

## **1.2. Porous carbon nanosheets**

One of the key factors for achieving high capacitive performance of carbonaceous material is creating effective structure with a high surface area and a short ionic diffusion path [10]. Porous carbon nanosheets have received considerable attention due to their two-dimensional sheets with a thin thickness which entails short ion transport distance. Thus far,

researchers have reported porous carbon nanosheets with various types of architectures and their capacitive performance as electrode materials in EDLCs [11-14]. However, the low energy density of carbon-based EDLCs is still a challenge for high-performance supercapacitor applications due to their electrostatic adsorption/desorption mechanism of electrolyte ions.

### **1.3. Nitrogen doping**

Nitrogen-doping is an attractive technique for increasing capacitance of carbonaceous materials because it enables additional charge storage through a surface faradic reaction without impairing the advantages of carbonaceous materials, such as their rate capability and long life cycle stability [15-18]. Nitrogen-doping into carbonaceous materials can be divided into two strategies: in-situ synthesis and post-heat-treatment [17, 19]. The in-situ synthesis usually includes carbonization of nitrogen-containing precursors such as polymer [20], biomass [21, 22], metal-organic frameworks [23]. But this strategy is limited to obtain the desired carbon structure and it would be required to use templates that are not suitable for large-scale production. In the post-heat-treatment, various carbon materials are treated with nitrogen-containing sources by diverse

methods including thermal annealing, plasma, arc-discharge approach, etc [24-27]. For example, M. Rybin and co-workers reported the fabrication of N-doped graphene through the ammonia plasma treatment for graphene obtained by CVD [24]. More recently, R. Liu and co-workers synthesized N, O-doped porous carbon nanosheets by an electrostatic self-assembly process using graphene oxide and polyacrylamide followed by KOH activation [25]. However, most of them required complex synthetic procedures, which could be the limitations for further developments. Therefore, a facile and effective post-heat-treatment method is needed for the development of obtaining N-doped porous carbon nanosheets.

#### **1.4. Redox additive in aqueous electrolyte**

Recently, there have been many reports on redox additive electrolytes to enhance supercapacitor performance, in which adding an active agent to the electrolyte led to a redox reaction [28-31]. Especially, an indole-based macromolecule with a low HOMO-LUMO gap (HLG) has been employed in supercapacitors as additive in electrolyte owing to their extended conjugated structure, which allowed fast charge transfer [29].

## 1.5. Objectives

Herein, N-doped porous carbon nanosheets were prepared using post-heat-treatment with melamine which is inexpensive and has relatively high nitrogen contents by mass. Condensation of melamine was induced by heat treatment with dwell time at certain temperatures which can improve the doping contents of nitrogen. As a result, the nitrogen ratio was improved around two time comparing with that without the dwell time during the heat treatment. In the three-electrode electrochemical test, the synthesized N-doped interconnected carbon nanosheets (NPCN) electrode delivered  $350 \text{ F g}^{-1}$  at a current density of  $1 \text{ A g}^{-1}$ , which is higher than that of pristine interconnected carbon nanosheets (PCN) electrode ( $279 \text{ F g}^{-1}$  at a current density of  $1 \text{ A g}^{-1}$ ). The indole based macromolecule containing electrolyte was also employed to as-synthesized NPCN electrodes based symmetric supercapacitor to improve electrochemical performance. The as-fabricated electrode delivered a specific capacitance of  $468 \text{ F g}^{-1}$  at a current density of  $1 \text{ A g}^{-1}$  and retain a capacitance of  $233 \text{ F g}^{-1}$  at a relatively high current density of  $20 \text{ A g}^{-1}$ .

## **2. Experimental Section**

### **2.1 Preparation of PCN**

Potassium citrate powder was placed on a tube furnace and heated up to 850 °C under Ar with a heating rate of 3 °C/min and maintained for 1 h. After heat-treatment, the resulting product was washed with 1.0 M HCl. Washed product was dried in a vacuum oven for 12 h. Finally, interconnected porous carbon nanosheets was obtained

### **2.2 Preparation of N-doped PCN**

PCN (50 mg) and melamine (50 mg, 200 mg) were mixed with toluene. NPCN was obtained via multistep with 300 °C for 1 h, 550 °C for 1 h, and 700 °C for 1 h. As a reference sample, heat treatment was conducted without the multistep at a heating rate of 5 °C/min. Finally, the products were collected after washing with water and ethanol three time. NPCN-11 for PCN to melamine ratio of 1:1, and NPCN-14 for PCN to melamine ratio of 1:4, respectively. The synthesized carbons with the multi-steps were named as NPCN-11D, and NPCN-14D, respectively.



### **2.3. Material characterization**

The obtained samples were analyzed via scanning electron microscopy (SEM, S-4800 Hitachi) and transmission electron microscopy (TEM, JEM-2010 JEOL). Fourier-transform infrared spectroscopy (FT-IR) was performed with Nicolet iS50 (Thermo Fisher Scientific). Gas adsorption/desorption analysis was carried out using the BELSORP-max instrument under nitrogen gas. The specific surface area (SSA) and total pore volume were calculated based on the Brunauer-Emmett-Teller theory and the pore distribution was evaluated based on the non-local density functional theory. Raman spectroscopy was carried out on a Raman spectrometer (DXR2xi). X-ray photoelectron spectroscopy (XPS) and elemental analysis (EA) were carried out by Thermo Escalab 250 Xi system (Thermo Scientific) and Flash 2000 analyzer, respectively. The Dynamic Light Scattering (DLS) data obtained by using a Zetasizer Nano ZS.

## 2.4. Electrochemical characterizations

The electrochemical performances of the prepared samples were evaluated via cyclic voltammetry (CV), galvanostatic charge/discharge (GCD) tests, and electrochemical impedance spectroscopy (EIS). The electrochemical performance was measured using a three-electrode configuration and a symmetric two-electrode configuration. For the three-electrode configuration, 5  $\mu\text{g}$  of active material was loaded on glassy carbon with a diameter of 3 mm to be used as working electrodes. Platinum mesh and Hg/HgO were used as the counter and reference electrodes, respectively. All the tests were performed in 6 M KOH. For the symmetric two-electrode configuration, a slurry containing 80 wt% of NPCN, 5 wt% of polyvinylidene fluoride, and 15 wt% of Super-P carbon was coated on the titanium foil to be used as the working electrode. The mass loading of active material was around 1  $\text{mg}/\text{cm}^2$ . A glassy fibrous membrane was used as a separator. Additionally, the indole based macromolecule containing electrolyte was obtained through electrochemical polymerization of dopamine solution followed by reference [29]. 0.5 M sulfuric acid with 0.025 M dopamine hydrochloride was transformed into a brown color solution through CV tests at a scan rate of 1000 mV using carbon cloths as cathode and anode.

The specific capacitances of the samples in the three-electrode ( $C_{three}$ , F g<sup>-1</sup>) and two symmetric electrode systems ( $C_{two}$ , F g<sup>-1</sup>) were calculated using the respective equations:

$$C_{three} = \frac{I\Delta t}{m\Delta V}$$

$$C_{two} = \frac{2I\Delta t}{m\Delta V}$$

where  $I$  is the galvanostatic discharge current,  $\Delta t$  is the discharging time,  $m$  is the mass of the active materials on the single electrode, and  $\Delta V$  is the voltage window.

The energy density was calculated using the following equation:

$$E_{symmetric} = \frac{C_{symmetric}\Delta V^2}{2 \times 3.6}$$

where  $C_{symmetric}$  is the specific capacitance of the two symmetric electrode systems. The power density was calculated using the following equation:

$$P_{symmetric} = \frac{E_{symmetric}}{\Delta t}$$

where  $\Delta t$  is the galvanostatic discharging time.

### 3. Results and Discussion

#### 3.1 Material analysis

The synthesis process of NPCN is shown in **Figure 1a**. The PCN which was obtained by the pyrolysis of potassium citrate at 850 °C was uniformly mixed with melamine. The obtained mixture was heated under Ar atmosphere up to 700 °C for nitrogen doping. Melamine is known to undergo rapid sublimation after 220 °C and this may cause a decrease in efficiency of nitrogen doping to PCN [32]. In order to minimize its sublimation, condensation of melamine is induced during heat treatment of the mixture through the appropriate dwell time near the temperature at which the melamine condensation occurs (**Figure 1b,c**) [33-36]. The mixture has passed by 1h at 300 °C, and 550 °C, respectively for the sequential condensation.

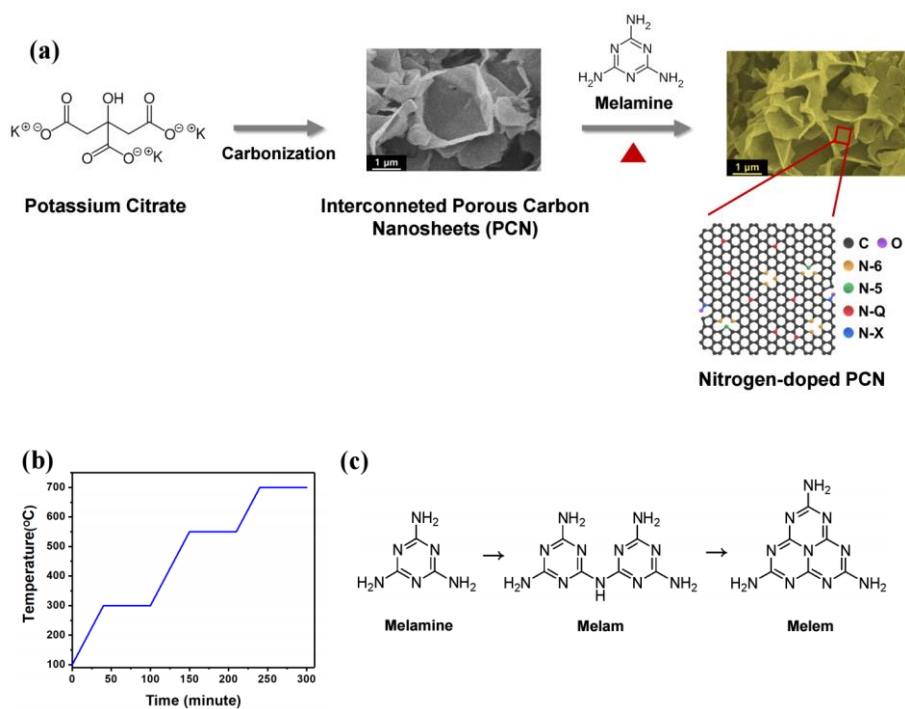


**Figure 1.** a) Synthesis process of NPCN. b) Heat treatment with the dwell time for condensation of melamine. c) Condensation process from melamine to melem.

To compare the extent of melamine condensation with respect to the implementation of dwell time during heat treatment, the samples were prepared via the two types of heat treatment (up to 580 °C) and denoted as NPCN-14D@580 for heat-treated with dwell time, and NPCN-14@580 for heat-treated without dwell time, respectively. The dwell effects in melamine were investigated by FT-IR in **Figure 2**. In the wavelength range of the N–H bond stretching at  $\sim 3100\text{ cm}^{-1}$ , the spectrum of NPCN-14D@580 exhibited a weaker peak than that of NPCN-14@580 [37]. Given that condensation of melamine releases ammonia gas, the reduced peak of NPCN-14D@580 may be attributed to a relatively condensed bonding structure. The peak at  $\sim 2350\text{ cm}^{-1}$  for C $\equiv$ N stretching mode which is found in melem that is more condensed structure than melem or melamine appeared only in the spectrum of NPCN-14D, which suggested NPCN-14D@580D has more condensed than NPCN-14@580 [37, 38].

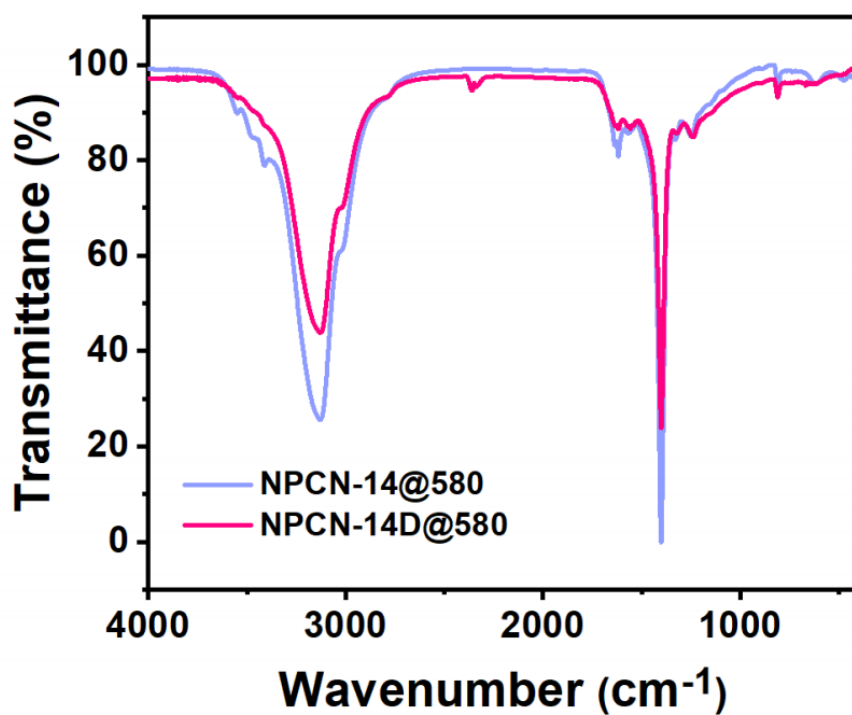


**Figure 2.** FTIR spectra of NPCN-14D@580 and NPCN-14@580.

The FE-SEM images of the as-prepared carbons are shown in **Figures**

**3.** The morphologies of all melamine-treated PCN are almost the same as those of bare PCN, which are composed of interconnected carbon nanosheets with dimensions of several micrometers. Although statistical analysis of the morphologies is required to evaluate the differences with more accuracy, this SEM images demonstrate that the post-heat treatment hardly changed the surface morphologies regardless of the method or initial ratio of carbon to melamine.



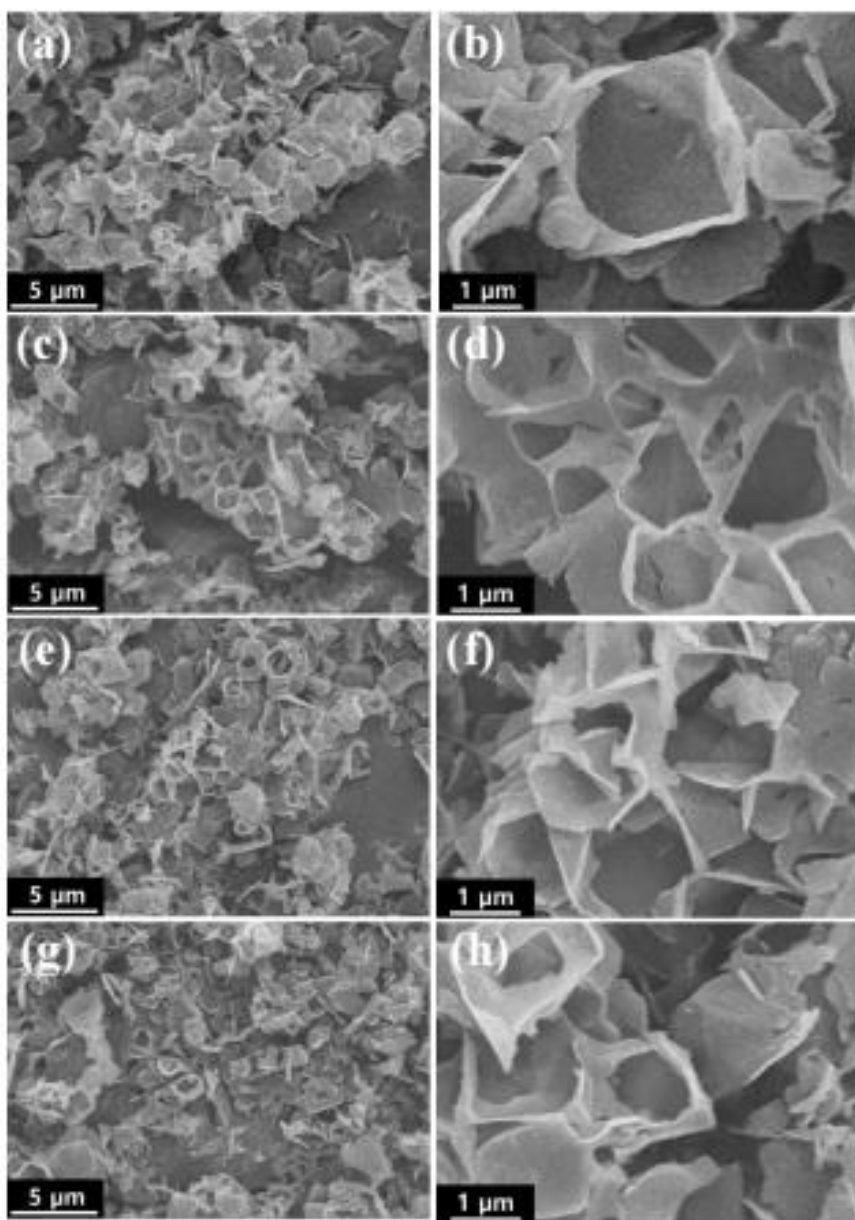


**Figure 3.** SEM images of the prepared samples of a, b) PCN, c, d) NPCN-11D, e, f) NPCN-14D g, h) NPCN-14 with low and relatively high-magnification.

TEM image of NPCN-14D in **Figure 4a** shows that the carbon nanosheet had randomly distributed micropores, which is consistent with previously published results [12]. The elemental distribution throughout the nanosheet-interconnected architecture of NPCN-14D was examined using X-ray elemental mapping, which indicated that C, O, and N were uniformly distributed on the surface of the carbon in **Figure 4b**.

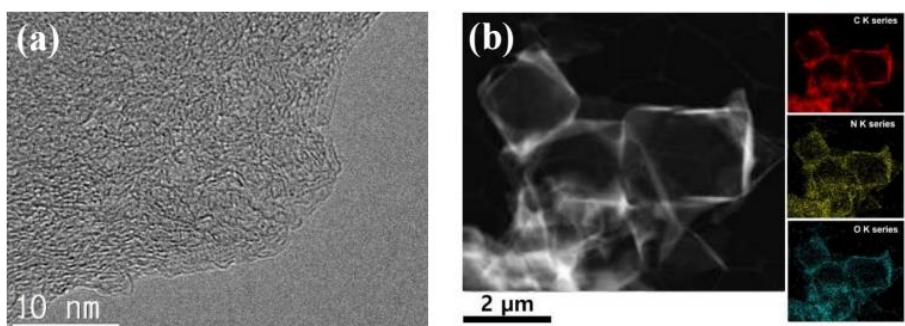


**Figure 4.** a) HR-TEM image and b) EDS mapping of NPCN-14D.

Nitrogen adsorption isotherms were conducted to further investigate the structural changes after nitrogen doping. As shown in **Figure 5a**, the nitrogen adsorption isotherms of NPCN-14D and PCN were typical type 1 isotherms, meaning that the structure was mainly composed of micropores. NPCN-14D had a specific surface area (SSA) of 1041.4 m<sup>2</sup> g<sup>-1</sup> and a total pore volume of 0.6321 cm<sup>3</sup> g<sup>-1</sup>. The structural parameters of NPCN-14D were slightly lower than those of PCN (SSA of 1247 m<sup>2</sup> g<sup>-1</sup>, a total pore volume of 0.7036 cm<sup>3</sup> g<sup>-1</sup>), which could be explained by the deposition of melamine condensate at the pore entrance during the annealing process [39, 40]. The pore-size distribution demonstrated that NPCN-14D had larger micropores than PCN (**Figure 5b**). This result could be supported by the fact that melamine-assisted nitrogen-doping could decrease micropores that were smaller than 5 Å and increase the larger micropore area [39]. Although the pore volume and SSA decreased slightly, NPCN-14D retained an efficient pore structure, considering that the micropore volume was still high and most of the reduced pore volume resulted from a reduction in very small micropores that were not accessible to electrolytes ions at high current density (**Table 1**).

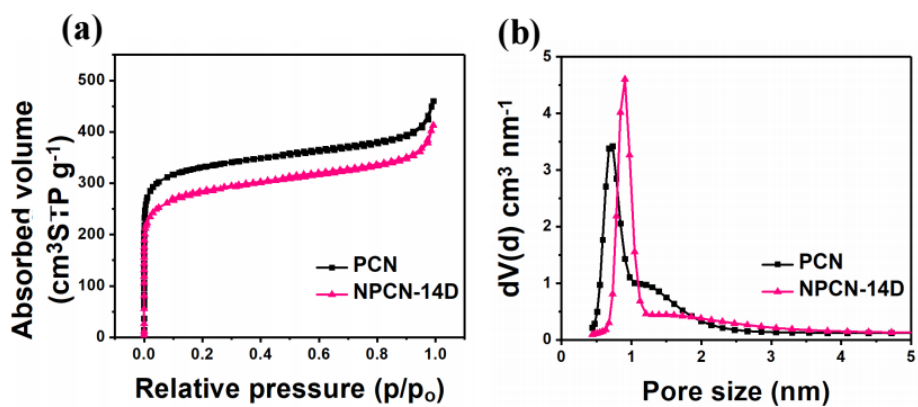


**Figure 5.** a) Nitrogen adsorption/desorption isotherm curves and b) Pore size distributions of PCN and NPCN-14D.

**Table 1.** Structural properties of PCN and NPCN-14D obtained from nitrogen adsorption/desorption analysis.

Sample name	Specific surface area [m <sup>2</sup> ·g <sup>-1</sup> ]	Mean diameter of pores [nm]	Pore volume [cm <sup>3</sup> ·g <sup>-1</sup> ]		
			Micropores	Meso- and macropores	Total
PCN	1247.3	2.2563	0.449	0.2546	0.7036
NPCN-14D	1041.4	2.4279	0.3662	0.2659	0.6321

Furthermore, Raman spectroscopy was performed to analyze the morphological changes in more detail (**Figure 6**). In the Raman spectra, all the samples presented two broad peaks at  $\sim 1350\text{ cm}^{-1}$  and  $1580\text{ cm}^{-1}$ , which are typical of carbonaceous materials [41]. The peak at  $1350\text{ cm}^{-1}$  (D-band) was related to structural defects, while the peak at  $1580\text{ cm}^{-1}$  (G-band) was ascribed to the  $\text{sp}^2$  carbon atoms arising from the in-plane vibration in graphitic planes [42]. The ratio of intensities of the two peaks,  $I_D/I_G$ , which indicates the degree of disorder, decreased in the order of PCN (0.97), NPCN-14 (1.01), NPCN-11D (1.00), and NPCN-14D (1.04), respectively. This result can be inferred that N-doping could cause structural disorder to the carbon network, suggesting that the doped-nitrogen ratio would be related to the  $I_D/I_G$  [27, 42].

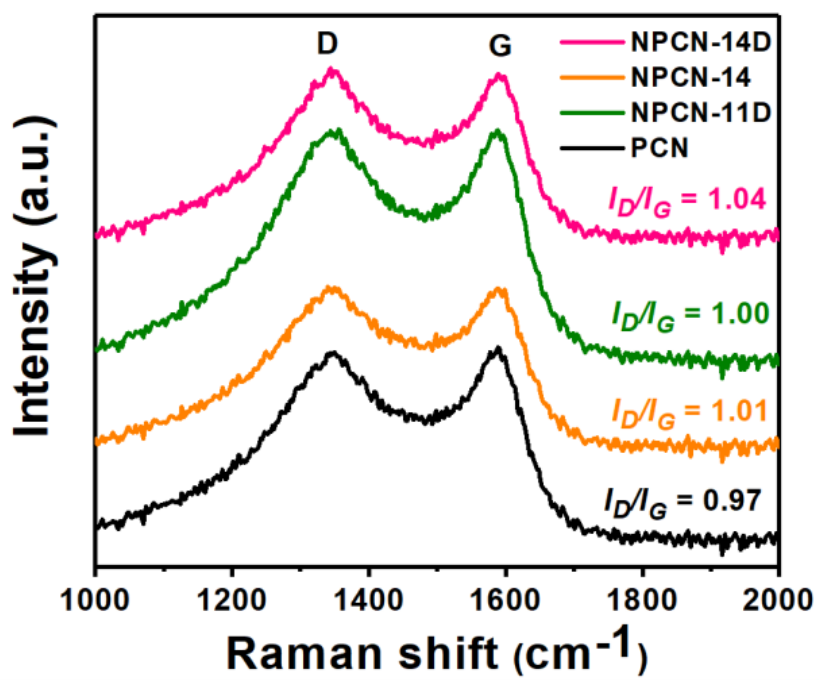


**Figure 6.** Raman spectra of NPCNs and PCN.



Moreover, XPS was conducted to investigate the surface chemistry of PCN and NPCN; the results are summarized in **Figure 7** and **Table 1**. The XPS survey spectrum revealed the presence of nitrogen in the NPCNs. As shown in **Table 1**, the nitrogen content of NPCN-14D (3 wt%) was higher than that of NPCN-11D (1.5 wt%) due to differences in the content of melamine in the initial mixture. Notably, the content of nitrogen in NPCN-14D was higher than that of NPCN-14 (1.4 wt%) with the same amount of melamine in the initial mixture, which can be interpreted as the result of the heat treatment containing dwell time increasing the efficiency of nitrogen doping. The nitrogen contents of NPCN-14N obtained by XPS measurement are almost similar to that of the EA measurement, indicating that NPCN-14N has an even nitrogen distribution. The high-resolution N1s XPS spectrum of NPCN-14D (**Figure 7b**) contained peaks at approximately 398 eV, 400 eV, 401.5 eV, and 405 eV, which corresponded to pyridinic (N-6), pyrrolic (N-5), quaternary (N-Q), and oxidized (N-X) forms, respectively [18]. **Figure 7c** shows the comparison of the nitrogen configurations of the samples. NPCN-14D had more N-Q than NPCN-11D and NPCN-14. In a previous study, researchers assumed that the higher contribution of N-Q on porous carbons treated with melamine was due to the chemical formula of

melamine and its condensed resin [39]. Considering this interpretation, this difference in the configuration of nitrogen may be related to the difference in the extent of condensation before the decomposition of melamine condensate in each sample. In the heat-treatment process for NPCN-14D, melamine was more condensed before decomposition owing to the dwell time compared to the process of NPCN-14. And that would be more condensed than in the process of NPCN-11D because of the higher amount of melamine in the initial mixture. The more polymerized the melamine, the greater the proportion of N-Q it contains. As a result, for NPCN-14D, melamine had more N-Q just before decomposition, which resulted in differences in the ratio of nitrogen configurations even after doping. The detailed mechanism of more N-Q in nitrogen-doping sources just before decomposition needs to be further investigated.

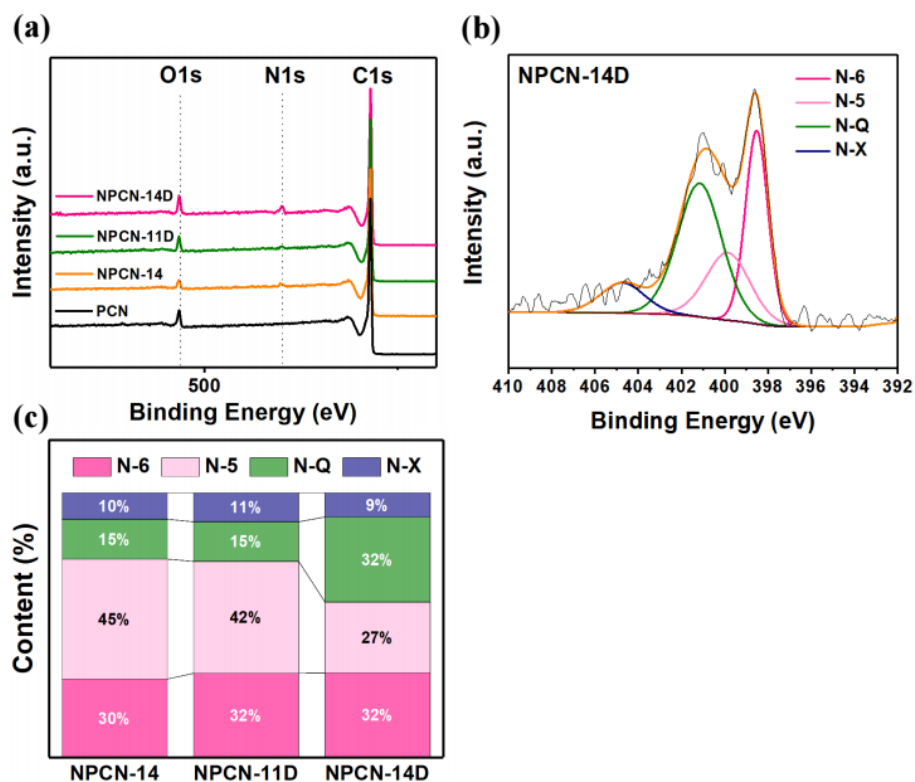


**Figure 7.** a) XPS survey spectra of NPCN and PCN. b) N1s high-resolution spectra of NPCN-14D. c) Nitrogen configurations of NPCN samples.

**Table 2.** Chemical compositions of PCN and NPCNs obtained from XPS and EA.

Sample code	Atomic (%)			
	C	N	O	H
PCN	95.3	0	4.7	-
NPCN-11D	94.5	1.5	4.0	-
NPCN-14D	92.3	3.0	4.7	-
NPCN-14	95.9	1.4	2.7	-
NPCN-14D(EA)	91.9	3.0	4.6	0.48

### 3.2. Electrochemical analysis

Electrochemical experiments were conducted to investigate the capacitive performance of the NPCN in a three-electrode system. The electrochemical performance of the samples synthesized with different amounts of melamine in the initial mixture was evaluated, as shown in **Figure 8a and b**. Figure 8a shows the CV curves of the samples at a scan rate of  $50 \text{ mV s}^{-1}$ . The area of the CV curve increased in the order of NPCN-14D, NPCN-11D, and PCN, respectively. Given that the surface area and pore volume of the NPCN samples were slightly lower than those of PCN, the increased area of the CV curve could be attributed to the faradic current derived from the nitrogen-containing functional groups in the NPCN samples. This is supported by that NPCN-14D, which had a higher nitrogen content, showed a wider CV area than NPCN-11D. To compare the rate capability, the specific capacitances of the samples at different current densities were calculated based on the discharging time (**Figure 8b**). NPCN-14D has achieved the highest a specific capacitance of  $350 \text{ F g}^{-1}$  at a current density of  $1 \text{ A g}^{-1}$ , which were higher than that of NPCN-11D ( $323 \text{ F g}^{-1}$ ) and PCN ( $279 \text{ F g}^{-1}$ ). NPCN-14D retained a capacitance of  $260 \text{ F g}^{-1}$  at a high current density of  $10 \text{ A g}^{-1}$ , with a rate performance of 74 %, which was higher than

those of NPCN-11D (212 F g<sup>-1</sup>, 70 %) and PC (181 F g<sup>-1</sup>, 65 %). **Figure 8c** shows the CV curves of NPCN-14D within the voltage range from -1.0 to 0 V<sub>Hg/HgO</sub> at different scan rates within 10 – 1000 mV s<sup>-1</sup>. The CV curve at a scan rate of 10 mV s<sup>-1</sup> exhibited a slightly deformed rectangle with a hump at a lower potential, indicating the faradic current that derived from N- and O-containing functional groups in NPCN-14D, which is consistent with the XPS and EA results. The CV curves at higher scan rates demonstrated a rectangular shape, which indicated that NPCN-14D had a high rate capability. The GCD curves at various current densities exhibited a similar trend to that of the CV curves (**Figure 8d**). Even at high current densities, there was no IR drop, which is related to internal resistance; this suggested that NPCN-14D had excellent capacitive properties.

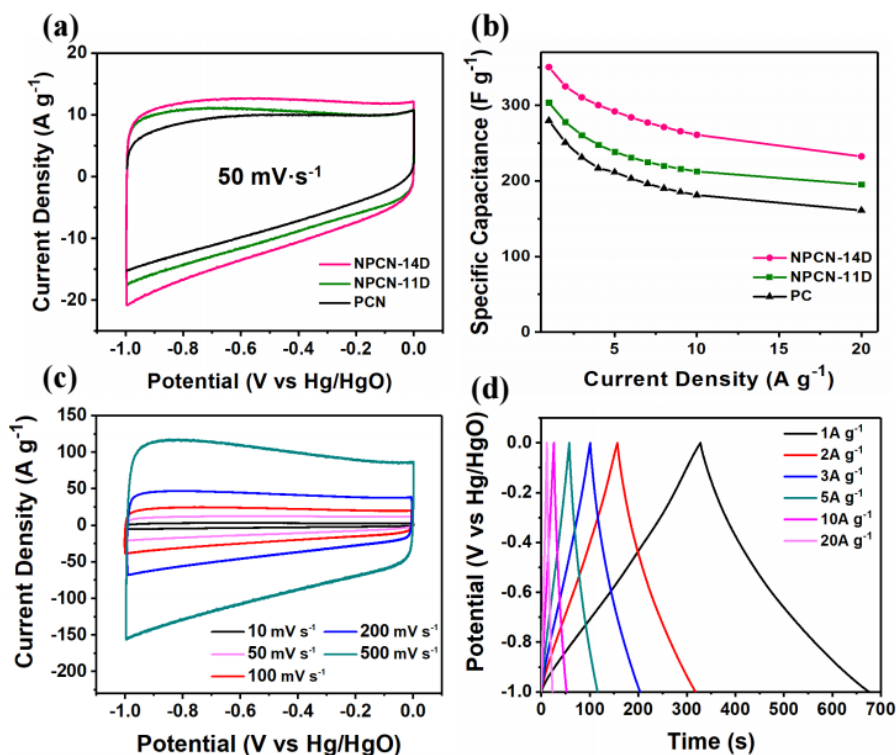


**Figure 8.** Electrochemical performances of PNC and NPCNs in the three-electrode system with 6M KOH electrolyte. a) CV curves at a scan rate of  $50 \text{ mV s}^{-1}$ , b) Specific capacitances at various current densities from 1 to  $20 \text{ A g}^{-1}$  of PCN, NPCN-11D, and NPCN-14D. c) CV curves at various scan rates from 10 to  $500 \text{ mV s}^{-1}$ , d) GCD curves at various current densities from 1 to  $20 \text{ A g}^{-1}$  of NPCN-14D.

To maximize the capacitive performance of NPCN-14D in practical cell applications, a symmetric supercapacitor using NPCN-14D as electrode material in a redox-mediated electrolyte was assembled. The indole-based macromolecule containing 5,6-dihydroxyindole/5,6-quinoneindole motifs for the redox additives in an aqueous electrolyte (IME) was synthesized through CV scanning at the rate of  $1000 \text{ mV s}^{-1}$ . The color of the dopamine solution transformed from transparent into brown after 24h. The change of the molecular size could be confirmed by DLS measurement (**Figure 9**). The size of the molecules was measured 100-250 nm after the electrochemical polymerization, which consistent with the previously reported results [29].



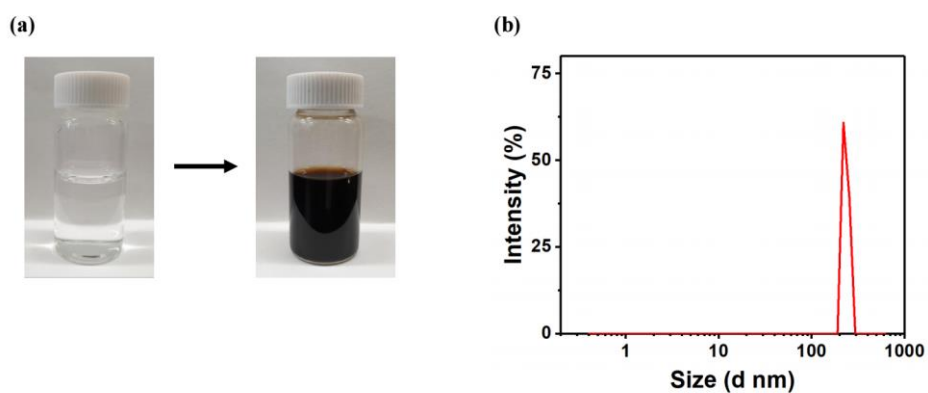


**Figure 9.** a) A color change of the dopamine solution resulting from the electrochemical polymerization and b) DLS measurement of IME.

The assembled symmetric supercapacitors were evaluated via several electrochemical tests. **Figure 10a** shows the CV curve of the fabricated cell at various scan rates ranging from  $25 \text{ mV s}^{-1}$  to  $1000 \text{ mV s}^{-1}$  with a potential window of  $0 - 1.2 \text{ V}$ . The curves at a relatively low scan rate displayed anodic and cathodic humps that were attributed to redox reactions. Notably, the rectangular shape was retained even at the high scan rate of  $1000 \text{ mV s}^{-1}$ , which indicated that the cell had a good rate performance. The GCD curves at different current densities had a deformed triangular shape, which was related to the redox reaction and corroborated the CV results (**Figure 10b**). **Figure 10c** shows the rate performance of the fabricated cell in IME and  $0.5\text{M H}_2\text{SO}_4$ . The electrode exhibited a capacitance of  $468 \text{ F g}^{-1}$  at a current density of  $1 \text{ A g}^{-1}$ . This value was relatively high compared to that in  $0.5\text{M H}_2\text{SO}_4$  ( $266 \text{ F g}^{-1}$ ), which appears to be due to the redox reaction of the additive in the electrolyte. Interestingly, the electrode retained a capacitance of  $233 \text{ F g}^{-1}$  at a relatively high current density of  $20 \text{ A g}^{-1}$  indicating that the macromolecules in the electrolyte caused a redox reaction even at very high current densities due to the small HLG. **Figure 10d** exhibits the Nyquist plot obtained via EIS in the assembled cell. In the Nyquist plot, the intersection between a high frequency line and  $Z'$  axis is related to

electrolyte resistance and the size of the semicircle in the middle-frequency area indicates the charge-transfer resistance of the cell. It can be seen that both of the electrolyte resistance and the charge-transfer resistance of the cell with IME is lower than these with 0.5 M H<sub>2</sub>SO<sub>4</sub>, which could be explained by the low HLG of IME. The polymerization of dopamine resulted in lower HLG of the molecules and the decreased HLG facilitated the electron transfer to acceptor, which increased ionic conductivity and allowed fast electron transfer within the molecules.

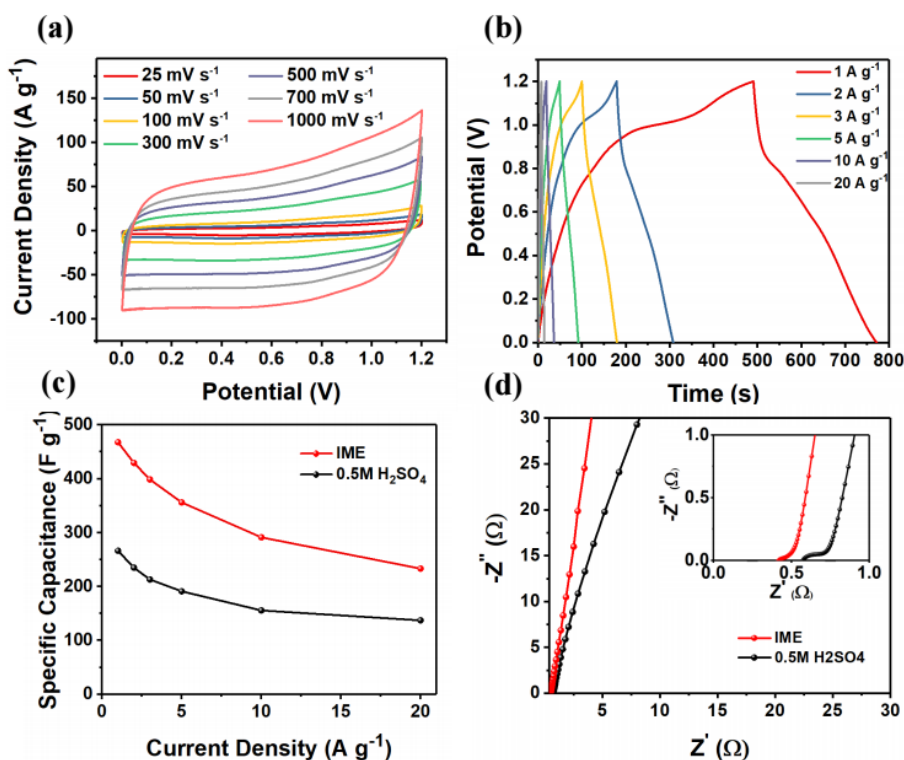


**Figure 10.** Electrochemical performances of NPCN-14D in the symmetric supercapacitors with indole based macromolecule electrolyte. a) CV curves at various scan rates from 25 to 1000  $\text{mV s}^{-1}$ . b) GCD curves and c) Specific capacitances at various current densities from 5 to 100  $\text{A g}^{-1}$ . d) Nyquist plot.

To confirm the stability of the assembled cell, a cycle test was conducted at a current density of  $20 \text{ A g}^{-1}$  (**Figure 11a**). The assembled cells maintained  $\sim 80 \%$  of their initial capacity after 3,000 cycles, indicating that the cells and redox electrolytes remained stable after repeated reactions at relatively high current densities. **Figure 11b** shows the energy-storage capacity and power performance of the cells in terms of energy and power densities. The assembled cell was able to store the energy density of  $1087 \text{ mWh kg}^{-1}$  at a power density of  $13.94 \text{ mW kg}^{-1}$  and  $371 \text{ Wh kg}^{-1}$  at the high power density of  $1395 \text{ W kg}^{-1}$ .

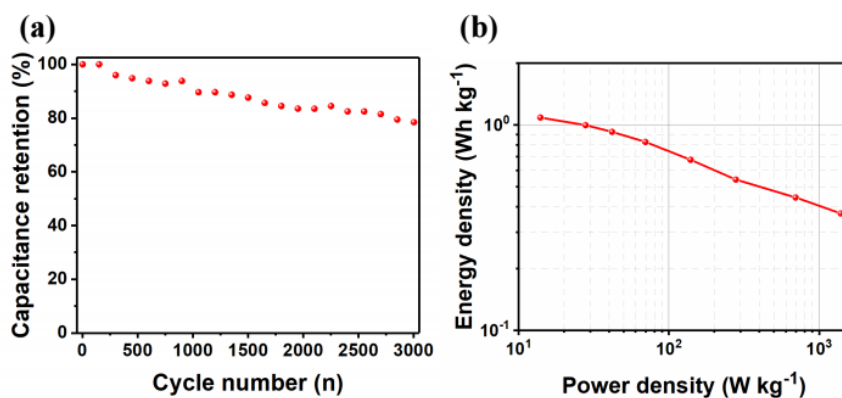


**Figure 11.** a) Cycle performance at 20 A g<sup>-1</sup>. b) Ragone plots of the symmetric supercapacitor.

## 4. Conclusions

In summary, N-doped interconnected porous carbon nanosheets derived from potassium citrate was prepared using post-heat-treatment with melamine. To induce melamine condensation during heat-treatment in the synthesis of NPCN, dwell time was set at the temperature of the condensation. The condensation of melamine was confirmed via FT-IR. As a result, the nitrogen-doping rate of the carbon synthesized with dwell time was around two time compared with that of the carbon without dwell time. The synthesized N-doped carbon showed an SSA of 1041.4  $\text{m}^2 \text{g}^{-1}$  and a total pore volume of 0.63  $\text{cm}^3 \text{g}^{-1}$  while maintaining the interconnected nanosheets structure. The NPCN-14D showed a specific capacitance of 350  $\text{F g}^{-1}$  at a current density of 1  $\text{A g}^{-1}$  in the three-electrode system. Moreover, the NPCN-14D was used as a symmetric supercapacitor paired with an indole-based macromolecule electrolyte, and it showed a specific capacitance of 468  $\text{F g}^{-1}$  at a current density of 1  $\text{A g}^{-1}$  and retain a specific capacitance of 233  $\text{F g}^{-1}$  at a relatively high current density of 20  $\text{A g}^{-1}$ .

## References

- [1] X. Zheng, J. Luo, W. Lv, D.W. Wang, Q.H. Yang, Two-Dimensional Porous Carbon: Synthesis and Ion-Transport Properties, *Adv Mater* 27 (2015) 5388-5395.
- [2] P. Simon, Y. Gogotsi, Materials for electrochemical capacitors, *Nat Mater* 7 (2008) 845-854.
- [3] R. Kotz, M. Carlen, Principles and applications of electrochemical capacitors, *Electrochimica Acta* 45 (2000) 2483-2498.
- [4] G. Wang, L. Zhang, J. Zhang, A review of electrode materials for electrochemical supercapacitors, *Chem Soc Rev* 41 (2012) 797-828.
- [5] L.L. Zhang, X.S. Zhao, Carbon-based materials as supercapacitor electrodes, *Chem Soc Rev* 38 (2009) 2520-2531.
- [6] X. Chen, R. Paul, L. Dai, Carbon-based supercapacitors for efficient energy storage, *National Science Review* 4 (2017) 453-489.
- [7] Z. Fan, J. Yan, L. Zhi, Q. Zhang, T. Wei, J. Feng, M. Zhang, W. Qian, F. Wei, A three-dimensional carbon nanotube/graphene sandwich and its application as electrode in supercapacitors, *Adv Mater* 22 (2010) 3723-3728.
- [8] Z. Fan, Y. Liu, J. Yan, G. Ning, Q. Wang, T. Wei, L. Zhi, F. Wei, Template-Directed Synthesis of Pillared-Porous Carbon Nanosheet



Architectures: High-Performance Electrode Materials for Supercapacitors, *Advanced Energy Materials* 2 (2012) 419-424.

[9] M.F. El-Kady, Y. Shao, R.B. Kaner, Graphene for batteries, supercapacitors and beyond, *Nature Reviews Materials* 1 (2016) 16033-16047.

[10] J. Wang, X. Yang, D. Wu, R. Fu, M.S. Dresselhaus, G. Dresselhaus, The porous structures of activated carbon aerogels and their effects on electrochemical performance, *Journal of Power Sources* 185 (2008) 589-594.

[11] H. Wang, Z. Xu, A. Kohandehghan, Z. Li, K. Cui, X. Tan, T.J. Stephenson, C.K. King'ondeu, C.M. Holt, B.C. Olsen, J.K. Tak, D. Harfield, A.O. Anyia, D. Mitlin, Interconnected carbon nanosheets derived from hemp for ultrafast supercapacitors with high energy, *Acs Nano* 7 (2013) 5131-5141.

[12] M. Sevilla, A.B. Fuertes, Direct Synthesis of Highly Porous Interconnected Carbon Nanosheets and Their Application as High-Performance Supercapacitors, *Acs Nano* 8 (2014) 5069-5078.

[13] X. Fan, C. Yu, J. Yang, Z. Ling, C. Hu, M. Zhang, J. Qiu, A Layered-Nanospace-Confinement Strategy for the Synthesis of Two-Dimensional Porous Carbon Nanosheets for High-Rate Performance Supercapacitors,

Advanced Energy Materials 5 (2015) 1401761-1401768.

[14] C. Chen, D. Yu, G. Zhao, B. Du, W. Tang, L. Sun, Y. Sun, F. Besenbacher, M. Yu, Three-dimensional scaffolding framework of porous carbon nanosheets derived from plant wastes for high-performance supercapacitors, Nano Energy 27 (2016) 377-389.

[15] K. Jurewicz, K. Babel, A. Żiółkowski, H. Wachowska, Ammoxidation of active carbons for improvement of supercapacitor characteristics, Electrochimica Acta 48 (2003) 1491-1498.

[16] G. Lota, B. Grzyb, H. Machnikowska, J. Machnikowski, E. Frackowiak, Effect of nitrogen in carbon electrode on the supercapacitor performance, Chemical Physics Letters 404 (2005) 53-58.

[17] K.N. Wood, R. O'Hayre, S. Pylypenko, Recent progress on nitrogen/carbon structures designed for use in energy and sustainability applications, Energy Environ. Sci. 7 (2014) 1212-1249.

[18] M. Inagaki, M. Toyoda, Y. Soneda, T. Morishita, Nitrogen-doped carbon materials, Carbon 132 (2018) 104-140.

[19] L. Hao, X. Li, L. Zhi, Carbonaceous electrode materials for supercapacitors, Adv Mater 25 (2013) 3899-904.

[20] Q. Liu, J. Zhong, Z. Sun, H. Mi, Cross-linked carbon networks constructed from N-doped nanosheets with enhanced performance for

supercapacitors, *Applied Surface Science* 396 (2017) 1326-1334.

[21] Y.-Y. Wang, B.-H. Hou, H.-Y. Lü, C.-L. Lü, X.-L. Wu Hierarchically Porous N-Doped Carbon Nanosheets Derived From Grapefruit Peels for High-Performance Supercapacitors, *ChemistrySelect* 1 (2016) 1441-1447.

[22] M. Chen, D. Yu, X. Zheng, X. Dong, Biomass based N-doped hierarchical porous carbon nanosheets for all-solid-state supercapacitors, *Journal of Energy Storage* 21 (2019) 105-112.

[23] D. Chen, S. Wang, Z. Zhang, H. Quan, Y. Wang, Y. Jiang, M.J. Hurlock, Q. Zhang, Molten NaCl-induced MOF-derived carbon-polyhedron decorated carbon-nanosheet with high defects and high N-doping for boosting the removal of carbamazepine from water, *Environmental Science: Nano* 7 (2020) 1205-1213.

[24] M. Rybin, A. Pereyaslavl'tsev, T. Vasilieva, V. Myasnikov, I. Sokolov, A. Pavlova, E. Obraztsova, A. Khomich, V. Ralchenko and E. Obraztsova, Efficient nitrogen doping of graphene by plasma treatment, *Carbon* 96 (2016) 196-202.

[25] R. Liu, Y. Wang, X. Wu, Two-dimensional nitrogen and oxygen Co-doping porous carbon nanosheets for high volumetric performance supercapacitors, *Microporous and Mesoporous Materials* 295 (2020)

109954-109961.

[26] Z.S. Wu, W.C. Ren, L. Xu, F. Li, H.M. Cheng, Doped Graphene Sheets As Anode Materials with Superhigh Rate and Large Capacity for Lithium Ion Batteries, *Acs Nano* 5 (2011) 5463-5471.

[27] L.S. Panchakarla, K.S. Subrahmanyam, S.K. Saha, A. Govindaraj, H.R. Krishnamurthy, U.V. Waghmare, C.N.R. Rao, Synthesis, Structure, and Properties of Boron- and Nitrogen-Doped Graphene, *Advanced Materials* 21 (2009) 4726-4730.

[28] S. Roldan, C. Blanco, M. Granda, R. Menendez, R. Santamaria, Towards a further generation of high-energy carbon-based capacitors by using redox-active electrolytes, *Angew Chem, Int. Ed.* 50 (2011) 1699-701.

[29] T. Xiong, W.S.V. Lee, L. Chen, T.L. Tan, X. Huang, J. Xue, Indole-based conjugated macromolecules as a redox-mediated electrolyte for an ultrahigh power supercapacitor, *Energy & Environmental Science* 10 (2017) 2441-2449.

[30] L. Yan, D. Li, T. Yan, G. Chen, L. Shi, Z. An, D. Zhang, Confining Redox Electrolytes in Functionalized Porous Carbon with Improved Energy Density for Supercapacitors, *ACS Appl Mater Interfaces* 10 (2018) 42494-42502.

- [31] K. Jayaramulu, D.P. Dubal, B. Nagar, V. Ranc, O. Tomanec, M. Petr, K.K.R. Datta, R. Zboril, P. Gomez-Romero, R.A. Fischer, Ultrathin Hierarchical Porous Carbon Nanosheets for High-Performance Supercapacitors and Redox Electrolyte Energy Storage, *Adv Mater* 30 (2018) 1705789-1705798.
- [32] S. Dyjak, W. Kiciński, A. Huczko, Thermite-driven melamine condensation to  $C_xN_yH_z$  graphitic ternary polymers: towards an instant, large-scale synthesis of g- $C_3N_4$ , *Journal of Materials Chemistry A* 3 (2015) 9621-9631.
- [33] Y.C. Zhao, D.L. Yu, H.W. Zhou, Y.J. Tian, O. Yanagisawa, Turbostratic carbon nitride prepared by pyrolysis of melamine, *Journal of Materials Science* 40 (2005) 2645-2647.
- [34] B.V. Lotsch, W. Schnick, New light on an old story: formation of melam during thermal condensation of melamine, *Chemistry* 13 (2007) 4956-4968.
- [35] A. Sattler, S. Pagano, M. Zeuner, A. Zurawski, D. Gunzelmann, J. Senker, K. Muller-Buschbaum, W. Schnick, Melamine-melam adduct phases: investigating the thermal condensation of melamine, *Chemistry* 15 (2009) 13161-13170.
- [36] H.B. Zheng, W. Chen, H. Gao, Y.Y. Wang, H.Y. Guo, S.Q. Guo, Z.L.

- Tang, J.Y. Zhang, Melem: an efficient metal-free luminescent material, *J. Mater. Chem. C* 5 (2017) 10746-10753.
- [37] D.L. Yu, J.L. He, Z.Y. Liu, B. Xu, D.C. Li, Y.J. Tian, Phase transformation of melamine at high pressure and temperature, *Journal of Materials Science* 4 (2007) 689-695.
- [38] W. Kulisch, M.P. Delplancke-Ogletree, J. Bulii, M. Jelinek, K. Jurek, J. Zemek, J. Klimovic, Characterization of magnetron sputtered carbon nitride films, *Diamond and related materials* 8 (1999) 1039-1045.
- [39] M. Seredych, D. Hulicova-Jurcakova, G.Q. Lu, T.J. Bandoz, Surface functional groups of carbons and the effects of their chemical character, density and accessibility to ions on electrochemical performance, *Carbon* 46 (2008) 1475-1488.
- [40] N.A. Travlou, C. Ushay, M. Seredych, E. Rodríguez-Castellón, T.J. Bandoz, Nitrogen-Doped Activated Carbon-Based Ammonia Sensors: Effect of Specific Surface Functional Groups on Carbon Electronic Properties, *ACS Sensors* 1 (2016) 591-599.
- [41] M.S. Dresselhaus, A. Jorio, M. Hofmann, G. Dresselhaus, R. Saito, Perspectives on carbon nanotubes and graphene Raman spectroscopy, *Nano Lett* 10 (2010) 751-758.
- [42] A.C. Ferrari, J. Robertson, Interpretation of Raman spectra of

disordered and amorphous carbon, Phys Rev B 61 (2000) 14095-14107.

## 국 문 초 록

다공성 탄소 나노시트는 제작이 간단하며 효율적인 구조를 통해 전해질 이온의 빠른 이동을 가능케 한다는 점에서 전기 이중층 커패시터 전극물질로 많은 주목을 받고 있다. 그렇지만 정전기적 흡착으로 전하를 저장하는 탄소 물질의 특성으로 전극물질로 활용 시 상대적으로 낮은 커패시턴스를 보인다는 점이 지적받고 있다. 본 연구에서는 다공성 탄소 나노시트에 효과적인 열처리 방법을 통해 질소를 도핑함으로써 용량을 향상시켰고, 합성된 탄소 물질을 산화/환원반응 첨가제가 들어간 전해질에 접목시켜 추가적인 성능 향상을 꾀하였다.

먼저, 포타슘 사이트레이트를 열분해하여 다공성 탄소 나노시트가 상호 연결된 형태의 탄소 물질을 합성하였다. 합성된 탄소 물질에 질소 도핑을 하기 위해 질소 함유량이 풍부한 멜라민을 탄소 물질과 교반하여 열처리하였는데, 열처리 과정 중 특정 온도에서 머무는 시간을 설정함으로써 멜라민의 중합을 유도하였다. 열처리 과정 중 발생한 중합은 멜라민의 손실을 최소화하였고, 그 결과 최종 질소 도핑 비율은 2배 가량 향상되었다. 질소 도핑된 탄소 물질의 전기화학적 특성을 3전극 상황에서 확인해 본 결과,  $1 \text{ A g}^{-1}$ 에서 도핑되지 않은 탄소 물질 대비 25 % 증가한  $360 \text{ F g}^{-1}$ 의 용량을 보였다. 또한, 대칭 2전극 상황에서는 산화/환원 첨가제가 들어간



전해질과 접목되어  $1 \text{ A g}^{-1}$ 에서  $468 \text{ F g}^{-1}$ 의 더욱 향상된 용량을 발현하였다.

본 연구는 다공성 탄소 나노시트에 질소 도핑을 하기 위해 멜라민의 중합반응을 활용한 효율적인 방법을 제시했다는 점과, 질소 도핑 및 산화/환원 첨가제가 들어간 전해질을 활용해서 다공성 탄소 나노시트의 커패시턴스 향상을 이뤄냈다는 점에서 의의가 있다.

**주요어:** 슈퍼커패시터, 상호 연결된 다공성 탄소 나노시트, 질소 도핑, 멜라민 중합, 산화/환원 첨가제가 포함된 수용액 전해질

학 번: 2018-24374



## 저작자표시-비영리-변경금지 2.0 대한민국

이용자는 아래의 조건을 따르는 경우에 한하여 자유롭게

- 이 저작물을 복제, 배포, 전송, 전시, 공연 및 방송할 수 있습니다.

다음과 같은 조건을 따라야 합니다:



저작자표시. 귀하는 원저작자를 표시하여야 합니다.



비영리. 귀하는 이 저작물을 영리 목적으로 이용할 수 없습니다.



변경금지. 귀하는 이 저작물을 개작, 변형 또는 가공할 수 없습니다.

- 귀하는, 이 저작물의 재이용이나 배포의 경우, 이 저작물에 적용된 이용허락조건을 명확하게 나타내어야 합니다.
- 저작권자로부터 별도의 허가를 받으면 이러한 조건들은 적용되지 않습니다.

저작권법에 따른 이용자의 권리는 위의 내용에 의하여 영향을 받지 않습니다.

이것은 [이용허락규약\(Legal Code\)](#)을 이해하기 쉽게 요약한 것입니다.

[Disclaimer](#)

공학석사 학위논문

**Facile Preparation of N-doped  
and Interconnected Porous  
Carbon Nanosheets for High-  
performance Supercapacitors  
with Redox Additives in Aqueous  
Electrolyte**

질소 도핑된 상호연결 구조의 다공성 탄소  
나노시트의 간편한 제작과 산화환원 첨가제가  
포함된 수용액 기반의 슈퍼커패시터에의 응용

2020년 8월

서울대학교 융합과학기술대학원

융합과학부 나노융합전공

김 덕 환

# **Facile Preparation of N-doped and Interconnected Porous Carbon Nanosheets for High- performance Supercapacitors with Redox Additives in Aqueous Electrolyte**

Deokhwan Kim

Program in Nano Science and Technology

Graduate School of Convergence Science & Technology

Seoul National University

## Abstract

N-doped porous carbon nanosheets have garnered research attention owing to their effective structure for fast ion diffusion and pseudocapacitive properties in supercapacitors. Herein, a facile method to incorporate nitrogen into interconnected porous carbon nanosheets with relatively high doping efficiency is proposed by inducing melamine condensation through appropriate dwell time. The as-prepared N-doped porous carbon material was studied as an electrode for the electrochemical double-layer capacitor. The carbon material delivered a specific capacitance of  $350 \text{ F g}^{-1}$  at a current density of  $1 \text{ A g}^{-1}$  in a three-electrode system. Furthermore, a symmetric supercapacitor device was fabricated using the N-doped interconnected carbon nanosheets with redox additives in aqueous electrolyte. Based on the redox reaction of the electrodes and electrolytes, the specific capacitance was measured  $468 \text{ F g}^{-1}$  at a current density of  $1 \text{ A g}^{-1}$  and  $233 \text{ F g}^{-1}$  at a relatively high current density of  $20 \text{ A g}^{-1}$ . This research provided an efficient method for nitrogen-doping into interconnected porous carbon nanosheets using melamine and showed potential of carbon electrode material for high-

performance supercapacitor applications with redox additives in aqueous electrolyte.

**Keywords:** Porous carbon nanosheets, Supercapacitors, N-doping, Redox additive electrolytes

**Student Number:** 2018-24374

# Contents

<b>1. Introduction .....</b>	<b>12</b>
1.1. Supercapacitor .....	12
1.2. Porous carbon nanosheets .....	12
1.3. Nitrogen doping .....	13
1.4. Redox additive in aqueous electrolyte .....	14
1.5. Objective .....	15
 <b>2. Experimental Section.....</b>	<b>16</b>
2.1. Preparation of PCN .....	16
2.2. Preparation of N-doped PCN .....	16
2.3. Material characterizations .....	17
2.4. Electrochemical characterizations .....	18
 <b>3. Results and Discussion .....</b>	<b>20</b>
3.1. Material analysis .....	20
3.2. Electrochemical analysis.....	37

<b>4. Conclusions .....</b>	<b>47</b>
-----------------------------	-----------

<b>References .....</b>	<b>48</b>
-------------------------	-----------

<b>국문 초록 (Abstract in Korean) .....</b>	<b>56</b>
---	-----------



## List of Figures

<b>Figure 1.</b>	a) Synthesis process of NPCN. b) Heat treatment with the dwell time for condensation of melamine. c) Condensation process from melamine to melem.....	21
<b>Figure 2.</b>	FTIR spectra of NPCN-14D@580 and NPCN-14@580... ..	23
<b>Figure 3.</b>	SEM images of the prepared samples of a, b) PCN, c, d) NPCN-11D, e, f) NPCN-14D g, h) NPCN-14 with low and relatively high-magnification.. ..	25
<b>Figure 4.</b>	a) HR-TEM image and b) EDS mapping of NPCN-14D..	27
<b>Figure 5.</b>	a) Nitrogen adsorption/desorption isotherm curves and b) Pore size distributions of PCN and NPCN-14D.. ..	29
<b>Figure 6.</b>	a) Raman spectra of NPCNs and PCN. ....	32

**Figure 7.** a) XPS survey spectra of NPCNs and PCN. b) Nitrogen configurations of NPCNs.. ..... 35

**Figure 8.** Electrochemical performances of PNC and NPCNs in the three-electrode system with 6M KOH electrolyte. a) CV curves at a scan rate of  $50 \text{ mV s}^{-1}$ , b) Specific capacitances at various current densities from 1 to  $20 \text{ A g}^{-1}$  of PCN, NPCN-11D, and NPCN-14D. c) CV curves at various scan rates from 10 to  $500 \text{ mV s}^{-1}$ , d) GCD curves at various current densities from 1 to  $20 \text{ A g}^{-1}$  of NPCN-14D..... 39

**Figure 9.** a) A color change of the dopamine solution resulting from the electrochemical polymerization and b) DLS measurement of IME.. ..... 41

**Figure 10.** Electrochemical performances of NPCN-14D in the symmetric supercapacitors with IME. a) CV curves at various scan rates from 25 to  $1000 \text{ mV s}^{-1}$ . b) GCD curves and c) Specific capacitances at various current densities from 5 to  $100 \text{ A g}^{-1}$ . d) Nyquist plot... ..... 44

<b>Figure 11.</b> a) Cycle performance at $20 \text{ A g}^{-1}$ and b) Ragone plots of the symmetric supercapacitor.. . . .	46
--	----

## List of Tables

<b>Table 1.</b>	Structural properties of PCN and NPCN-14D obtained from nitrogen adsorption/desorption analysis... ..	30
<b>Table 2.</b>	Chemical compositions of PCN and NPCNs obtained from XPS and EA.....	36

# **1. Introduction**

## **1.1. Supercapacitors**

Supercapacitors are receiving considerable attention as next-generation energy-storage devices because of their high power characteristics and long lifespan [1, 2]. There are two kinds of supercapacitors based on the charge storage mechanism: electrochemical double-layer capacitors (EDLCs) and pseudo-capacitors [3, 4]. The EDLCs store the charge through adsorption/desorption of electrolyte ions to the electrode surface, while in pseudo-capacitors, the charge is stored by a reversible faradic reaction. Carbonaceous materials have been mainly used as electrode materials in EDLCs owing to their high specific surface area, good electrical conductivity, and chemical stability [5-9].

## **1.2. Porous carbon nanosheets**

One of the key factors for achieving high capacitive performance of carbonaceous material is creating effective structure with a high surface area and a short ionic diffusion path [10]. Porous carbon nanosheets have received considerable attention due to their two-dimensional sheets with a thin thickness which entails short ion transport distance. Thus far,

researchers have reported porous carbon nanosheets with various types of architectures and their capacitive performance as electrode materials in EDLCs [11-14]. However, the low energy density of carbon-based EDLCs is still a challenge for high-performance supercapacitor applications due to their electrostatic adsorption/desorption mechanism of electrolyte ions.

### **1.3. Nitrogen doping**

Nitrogen-doping is an attractive technique for increasing capacitance of carbonaceous materials because it enables additional charge storage through a surface faradic reaction without impairing the advantages of carbonaceous materials, such as their rate capability and long life cycle stability [15-18]. Nitrogen-doping into carbonaceous materials can be divided into two strategies: in-situ synthesis and post-heat-treatment [17, 19]. The in-situ synthesis usually includes carbonization of nitrogen-containing precursors such as polymer [20], biomass [21, 22], metal-organic frameworks [23]. But this strategy is limited to obtain the desired carbon structure and it would be required to use templates that are not suitable for large-scale production. In the post-heat-treatment, various carbon materials are treated with nitrogen-containing sources by diverse

methods including thermal annealing, plasma, arc-discharge approach, etc [24-27]. For example, M. Rybin and co-workers reported the fabrication of N-doped graphene through the ammonia plasma treatment for graphene obtained by CVD [24]. More recently, R. Liu and co-workers synthesized N, O-doped porous carbon nanosheets by an electrostatic self-assembly process using graphene oxide and polyacrylamide followed by KOH activation [25]. However, most of them required complex synthetic procedures, which could be the limitations for further developments. Therefore, a facile and effective post-heat-treatment method is needed for the development of obtaining N-doped porous carbon nanosheets.

#### **1.4. Redox additive in aqueous electrolyte**

Recently, there have been many reports on redox additive electrolytes to enhance supercapacitor performance, in which adding an active agent to the electrolyte led to a redox reaction [28-31]. Especially, an indole-based macromolecule with a low HOMO-LUMO gap (HLG) has been employed in supercapacitors as additive in electrolyte owing to their extended conjugated structure, which allowed fast charge transfer [29].

## 1.5. Objectives

Herein, N-doped porous carbon nanosheets were prepared using post-heat-treatment with melamine which is inexpensive and has relatively high nitrogen contents by mass. Condensation of melamine was induced by heat treatment with dwell time at certain temperatures which can improve the doping contents of nitrogen. As a result, the nitrogen ratio was improved around two time comparing with that without the dwell time during the heat treatment. In the three-electrode electrochemical test, the synthesized N-doped interconnected carbon nanosheets (NPCN) electrode delivered  $350 \text{ F g}^{-1}$  at a current density of  $1 \text{ A g}^{-1}$ , which is higher than that of pristine interconnected carbon nanosheets (PCN) electrode ( $279 \text{ F g}^{-1}$  at a current density of  $1 \text{ A g}^{-1}$ ). The indole based macromolecule containing electrolyte was also employed to as-synthesized NPCN electrodes based symmetric supercapacitor to improve electrochemical performance. The as-fabricated electrode delivered a specific capacitance of  $468 \text{ F g}^{-1}$  at a current density of  $1 \text{ A g}^{-1}$  and retain a capacitance of  $233 \text{ F g}^{-1}$  at a relatively high current density of  $20 \text{ A g}^{-1}$ .



## **2. Experimental Section**

### **2.1 Preparation of PCN**

Potassium citrate powder was placed on a tube furnace and heated up to 850 °C under Ar with a heating rate of 3 °C/min and maintained for 1 h. After heat-treatment, the resulting product was washed with 1.0 M HCl. Washed product was dried in a vacuum oven for 12 h. Finally, interconnected porous carbon nanosheets was obtained

### **2.2 Preparation of N-doped PCN**

PCN (50 mg) and melamine (50 mg, 200 mg) were mixed with toluene. NPCN was obtained via multistep with 300 °C for 1 h, 550 °C for 1 h, and 700 °C for 1 h. As a reference sample, heat treatment was conducted without the multistep at a heating rate of 5 °C/min. Finally, the products were collected after washing with water and ethanol three time. NPCN-11 for PCN to melamine ratio of 1:1, and NPCN-14 for PCN to melamine ratio of 1:4, respectively. The synthesized carbons with the multi-steps were named as NPCN-11D, and NPCN-14D, respectively.

### **2.3. Material characterization**

The obtained samples were analyzed via scanning electron microscopy (SEM, S-4800 Hitachi) and transmission electron microscopy (TEM, JEM-2010 JEOL). Fourier-transform infrared spectroscopy (FT-IR) was performed with Nicolet iS50 (Thermo Fisher Scientific). Gas adsorption/desorption analysis was carried out using the BELSORP-max instrument under nitrogen gas. The specific surface area (SSA) and total pore volume were calculated based on the Brunauer-Emmett-Teller theory and the pore distribution was evaluated based on the non-local density functional theory. Raman spectroscopy was carried out on a Raman spectrometer (DXR2xi). X-ray photoelectron spectroscopy (XPS) and elemental analysis (EA) were carried out by Thermo Escalab 250 Xi system (Thermo Scientific) and Flash 2000 analyzer, respectively. The Dynamic Light Scattering (DLS) data obtained by using a Zetasizer Nano ZS.

## 2.4. Electrochemical characterizations

The electrochemical performances of the prepared samples were evaluated via cyclic voltammetry (CV), galvanostatic charge/discharge (GCD) tests, and electrochemical impedance spectroscopy (EIS). The electrochemical performance was measured using a three-electrode configuration and a symmetric two-electrode configuration. For the three-electrode configuration, 5  $\mu\text{g}$  of active material was loaded on glassy carbon with a diameter of 3 mm to be used as working electrodes. Platinum mesh and Hg/HgO were used as the counter and reference electrodes, respectively. All the tests were performed in 6 M KOH. For the symmetric two-electrode configuration, a slurry containing 80 wt% of NPCN, 5 wt% of polyvinylidene fluoride, and 15 wt% of Super-P carbon was coated on the titanium foil to be used as the working electrode. The mass loading of active material was around 1  $\text{mg}/\text{cm}^2$ . A glassy fibrous membrane was used as a separator. Additionally, the indole based macromolecule containing electrolyte was obtained through electrochemical polymerization of dopamine solution followed by reference [29]. 0.5 M sulfuric acid with 0.025 M dopamine hydrochloride was transformed into a brown color solution through CV tests at a scan rate of 1000 mV using carbon cloths as cathode and anode.

The specific capacitances of the samples in the three-electrode ( $C_{three}$ , F g<sup>-1</sup>) and two symmetric electrode systems ( $C_{two}$ , F g<sup>-1</sup>) were calculated using the respective equations:

$$C_{three} = \frac{I\Delta t}{m\Delta V}$$

$$C_{two} = \frac{2I\Delta t}{m\Delta V}$$

where  $I$  is the galvanostatic discharge current,  $\Delta t$  is the discharging time,  $m$  is the mass of the active materials on the single electrode, and  $\Delta V$  is the voltage window.

The energy density was calculated using the following equation:

$$E_{symmetric} = \frac{C_{symmetric}\Delta V^2}{2 \times 3.6}$$

where  $C_{symmetric}$  is the specific capacitance of the two symmetric electrode systems. The power density was calculated using the following equation:

$$P_{symmetric} = \frac{E_{symmetric}}{\Delta t}$$

where  $\Delta t$  is the galvanostatic discharging time.

### 3. Results and Discussion

#### 3.1 Material analysis

The synthesis process of NPCN is shown in **Figure 1a**. The PCN which was obtained by the pyrolysis of potassium citrate at 850 °C was uniformly mixed with melamine. The obtained mixture was heated under Ar atmosphere up to 700 °C for nitrogen doping. Melamine is known to undergo rapid sublimation after 220 °C and this may cause a decrease in efficiency of nitrogen doping to PCN [32]. In order to minimize its sublimation, condensation of melamine is induced during heat treatment of the mixture through the appropriate dwell time near the temperature at which the melamine condensation occurs (**Figure 1b,c**) [33-36]. The mixture has passed by 1h at 300 °C, and 550 °C, respectively for the sequential condensation.

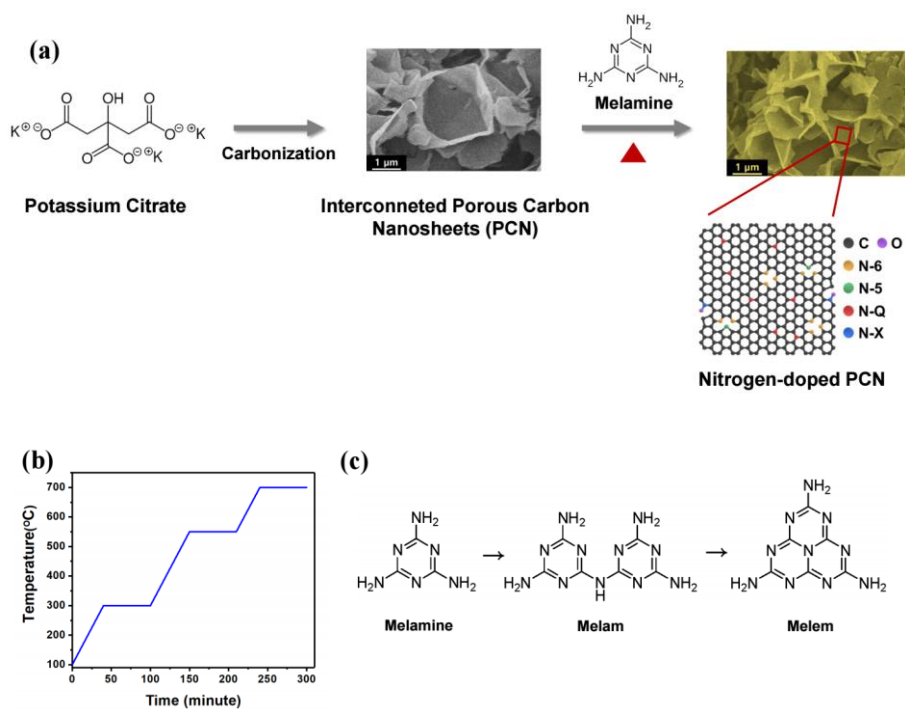


**Figure 1.** a) Synthesis process of NPCN. b) Heat treatment with the dwell time for condensation of melamine. c) Condensation process from melamine to melem.

To compare the extent of melamine condensation with respect to the implementation of dwell time during heat treatment, the samples were prepared via the two types of heat treatment (up to 580 °C) and denoted as NPCN-14D@580 for heat-treated with dwell time, and NPCN-14@580 for heat-treated without dwell time, respectively. The dwell effects in melamine were investigated by FT-IR in **Figure 2**. In the wavelength range of the N–H bond stretching at  $\sim 3100\text{ cm}^{-1}$ , the spectrum of NPCN-14D@580 exhibited a weaker peak than that of NPCN-14@580 [37]. Given that condensation of melamine releases ammonia gas, the reduced peak of NPCN-14D@580 may be attributed to a relatively condensed bonding structure. The peak at  $\sim 2350\text{ cm}^{-1}$  for C $\equiv$ N stretching mode which is found in melem that is more condensed structure than melem or melamine appeared only in the spectrum of NPCN-14D, which suggested NPCN-14D@580D has more condensed than NPCN-14@580 [37, 38].

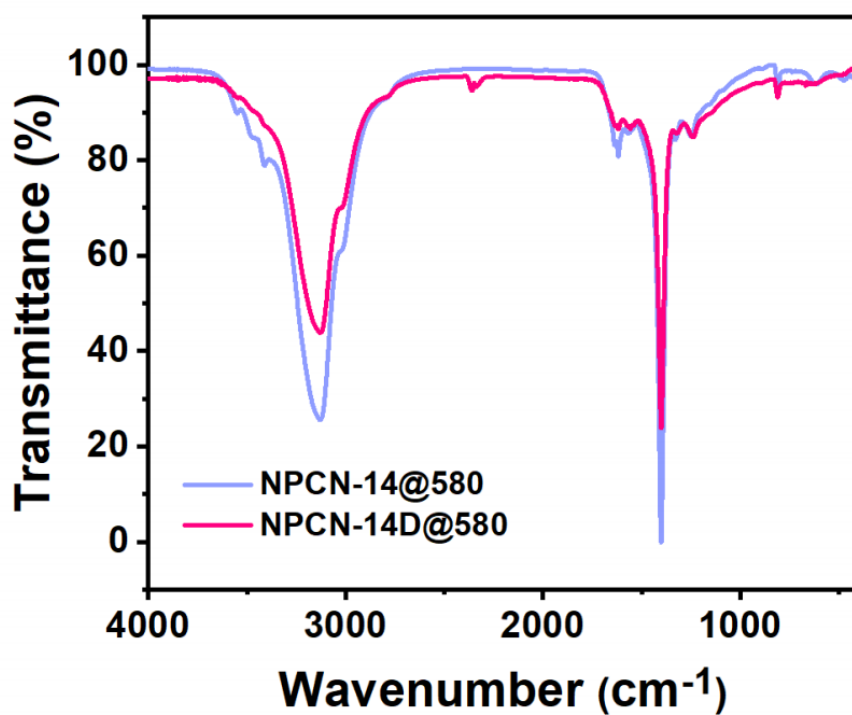


**Figure 2.** FTIR spectra of NPCN-14D@580 and NPCN-14@580.



The FE-SEM images of the as-prepared carbons are shown in **Figures 3**. The morphologies of all melamine-treated PCN are almost the same as those of bare PCN, which are composed of interconnected carbon nanosheets with dimensions of several micrometers. Although statistical analysis of the morphologies is required to evaluate the differences with more accuracy, this SEM images demonstrate that the post-heat treatment hardly changed the surface morphologies regardless of the method or initial ratio of carbon to melamine.

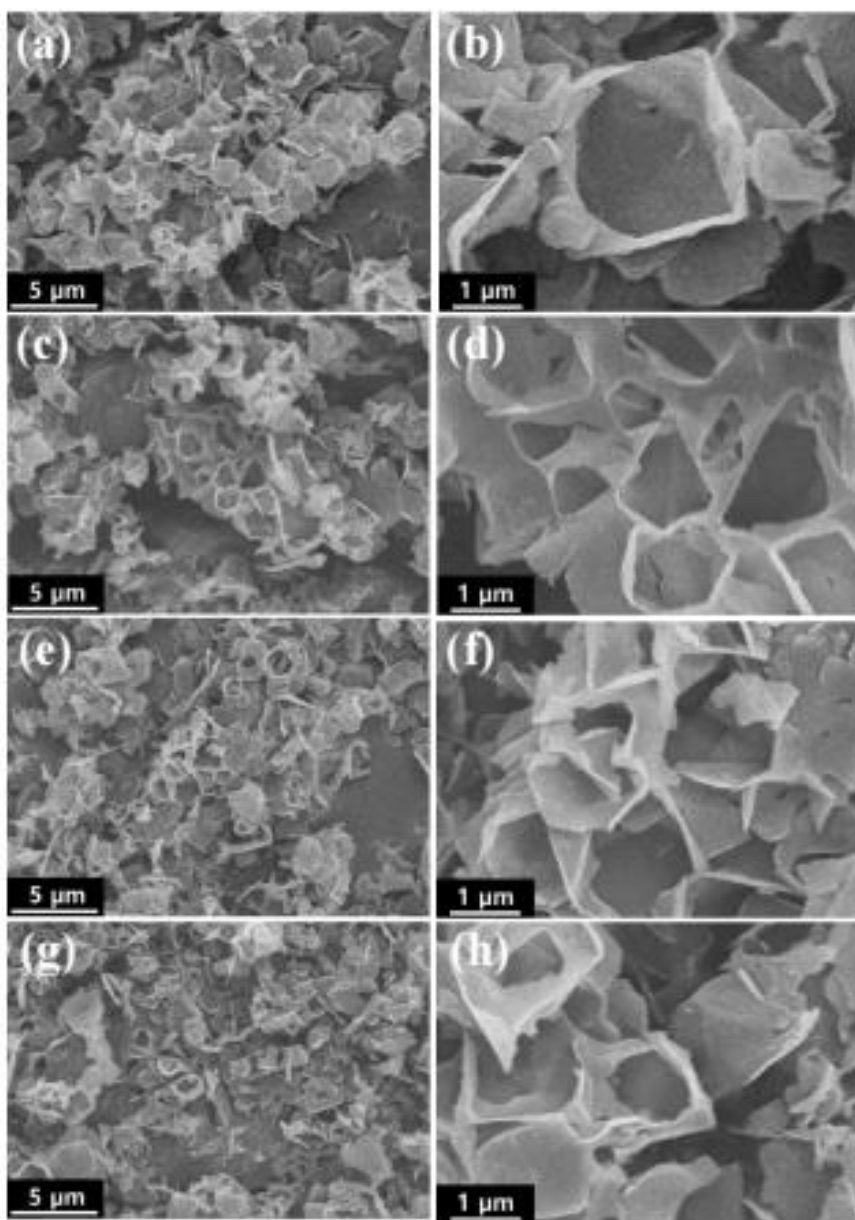


**Figure 3.** SEM images of the prepared samples of a, b) PCN, c, d) NPCN-11D, e, f) NPCN-14D g, h) NPCN-14 with low and relatively high-magnification.

TEM image of NPCN-14D in **Figure 4a** shows that the carbon nanosheet had randomly distributed micropores, which is consistent with previously published results [12]. The elemental distribution throughout the nanosheet-interconnected architecture of NPCN-14D was examined using X-ray elemental mapping, which indicated that C, O, and N were uniformly distributed on the surface of the carbon in **Figure 4b**.

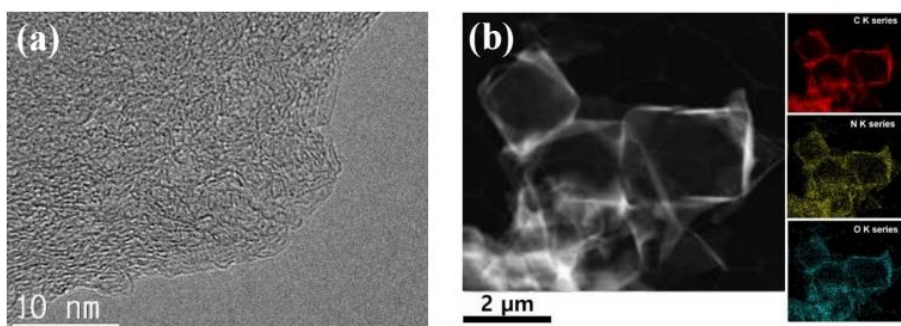


**Figure 4.** a) HR-TEM image and b) EDS mapping of NPCN-14D.

Nitrogen adsorption isotherms were conducted to further investigate the structural changes after nitrogen doping. As shown in **Figure 5a**, the nitrogen adsorption isotherms of NPCN-14D and PCN were typical type 1 isotherms, meaning that the structure was mainly composed of micropores. NPCN-14D had a specific surface area (SSA) of 1041.4 m<sup>2</sup> g<sup>-1</sup> and a total pore volume of 0.6321 cm<sup>3</sup> g<sup>-1</sup>. The structural parameters of NPCN-14D were slightly lower than those of PCN (SSA of 1247 m<sup>2</sup> g<sup>-1</sup>, a total pore volume of 0.7036 cm<sup>3</sup> g<sup>-1</sup>), which could be explained by the deposition of melamine condensate at the pore entrance during the annealing process [39, 40]. The pore-size distribution demonstrated that NPCN-14D had larger micropores than PCN (**Figure 5b**). This result could be supported by the fact that melamine-assisted nitrogen-doping could decrease micropores that were smaller than 5 Å and increase the larger micropore area [39]. Although the pore volume and SSA decreased slightly, NPCN-14D retained an efficient pore structure, considering that the micropore volume was still high and most of the reduced pore volume resulted from a reduction in very small micropores that were not accessible to electrolytes ions at high current density (**Table 1**).

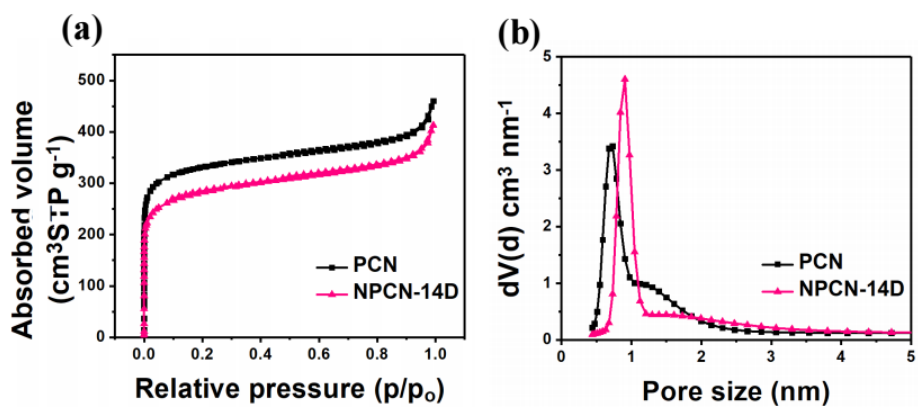


**Figure 5.** a) Nitrogen adsorption/desorption isotherm curves and b) Pore size distributions of PCN and NPCN-14D.

**Table 1.** Structural properties of PCN and NPCN-14D obtained from nitrogen adsorption/desorption analysis.

Sample name	Specific surface area [m <sup>2</sup> ·g <sup>-1</sup> ]	Mean diameter of pores [nm]	Pore volume [cm <sup>3</sup> ·g <sup>-1</sup> ]		
			Micropores	Meso- and macropores	Total
PCN	1247.3	2.2563	0.449	0.2546	0.7036
NPCN-14D	1041.4	2.4279	0.3662	0.2659	0.6321

Furthermore, Raman spectroscopy was performed to analyze the morphological changes in more detail (**Figure 6**). In the Raman spectra, all the samples presented two broad peaks at  $\sim 1350\text{ cm}^{-1}$  and  $1580\text{ cm}^{-1}$ , which are typical of carbonaceous materials [41]. The peak at  $1350\text{ cm}^{-1}$  (D-band) was related to structural defects, while the peak at  $1580\text{ cm}^{-1}$  (G-band) was ascribed to the  $\text{sp}^2$  carbon atoms arising from the in-plane vibration in graphitic planes [42]. The ratio of intensities of the two peaks,  $I_D/I_G$ , which indicates the degree of disorder, decreased in the order of PCN (0.97), NPCN-14 (1.01), NPCN-11D (1.00), and NPCN-14D (1.04), respectively. This result can be inferred that N-doping could cause structural disorder to the carbon network, suggesting that the doped-nitrogen ratio would be related to the  $I_D/I_G$  [27, 42].



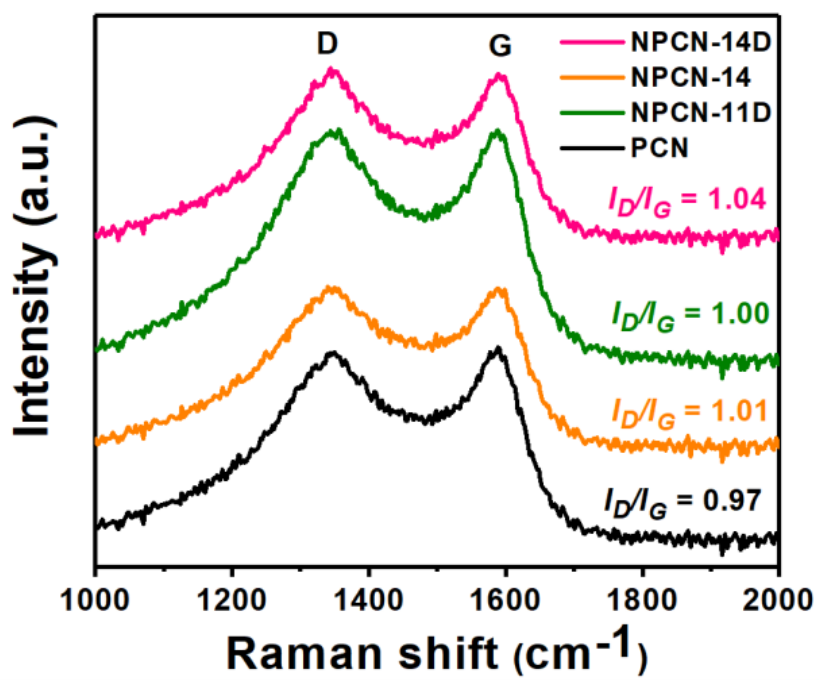


**Figure 6.** Raman spectra of NPCNs and PCN.

Moreover, XPS was conducted to investigate the surface chemistry of PCN and NPCN; the results are summarized in **Figure 7** and **Table 1**. The XPS survey spectrum revealed the presence of nitrogen in the NPCNs. As shown in **Table 1**, the nitrogen content of NPCN-14D (3 wt%) was higher than that of NPCN-11D (1.5 wt%) due to differences in the content of melamine in the initial mixture. Notably, the content of nitrogen in NPCN-14D was higher than that of NPCN-14 (1.4 wt%) with the same amount of melamine in the initial mixture, which can be interpreted as the result of the heat treatment containing dwell time increasing the efficiency of nitrogen doping. The nitrogen contents of NPCN-14N obtained by XPS measurement are almost similar to that of the EA measurement, indicating that NPCN-14N has an even nitrogen distribution. The high-resolution N1s XPS spectrum of NPCN-14D (**Figure 7b**) contained peaks at approximately 398 eV, 400 eV, 401.5 eV, and 405 eV, which corresponded to pyridinic (N-6), pyrrolic (N-5), quaternary (N-Q), and oxidized (N-X) forms, respectively [18]. **Figure 7c** shows the comparison of the nitrogen configurations of the samples. NPCN-14D had more N-Q than NPCN-11D and NPCN-14. In a previous study, researchers assumed that the higher contribution of N-Q on porous carbons treated with melamine was due to the chemical formula of

melamine and its condensed resin [39]. Considering this interpretation, this difference in the configuration of nitrogen may be related to the difference in the extent of condensation before the decomposition of melamine condensate in each sample. In the heat-treatment process for NPCN-14D, melamine was more condensed before decomposition owing to the dwell time compared to the process of NPCN-14. And that would be more condensed than in the process of NPCN-11D because of the higher amount of melamine in the initial mixture. The more polymerized the melamine, the greater the proportion of N-Q it contains. As a result, for NPCN-14D, melamine had more N-Q just before decomposition, which resulted in differences in the ratio of nitrogen configurations even after doping. The detailed mechanism of more N-Q in nitrogen-doping sources just before decomposition needs to be further investigated.

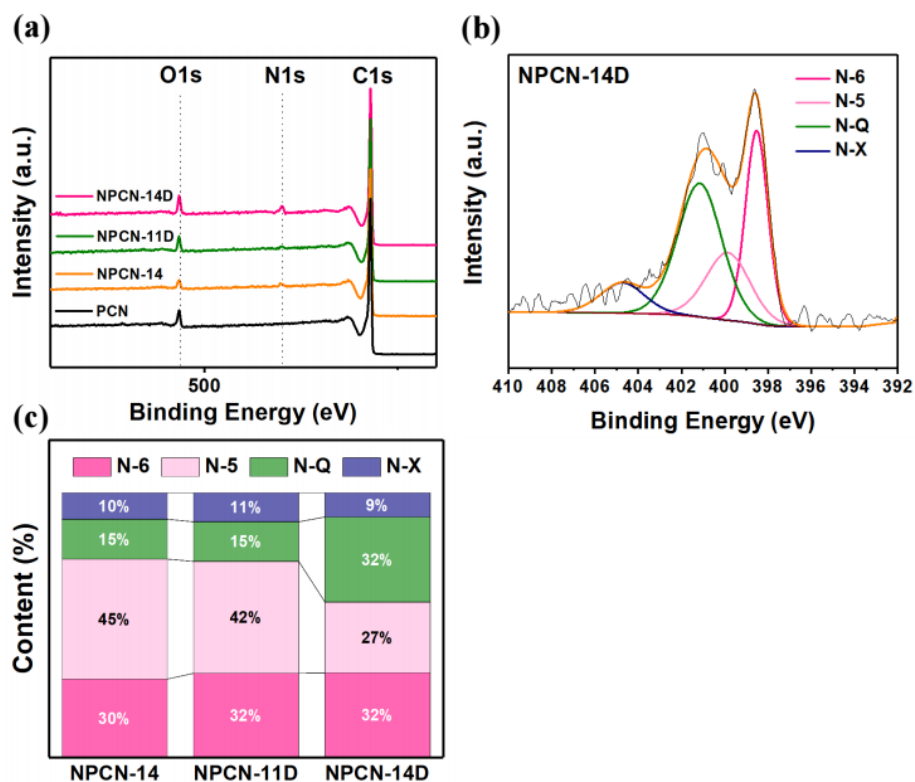


**Figure 7.** a) XPS survey spectra of NPCN and PCN. b) N1s high-resolution spectra of NPCN-14D. c) Nitrogen configurations of NPCN samples.

**Table 2.** Chemical compositions of PCN and NPCNs obtained from XPS and EA.

Sample code	Atomic (%)			
	C	N	O	H
PCN	95.3	0	4.7	-
NPCN-11D	94.5	1.5	4.0	-
NPCN-14D	92.3	3.0	4.7	-
NPCN-14	95.9	1.4	2.7	-
NPCN-14D(EA)	91.9	3.0	4.6	0.48

### 3.2. Electrochemical analysis

Electrochemical experiments were conducted to investigate the capacitive performance of the NPCN in a three-electrode system. The electrochemical performance of the samples synthesized with different amounts of melamine in the initial mixture was evaluated, as shown in **Figure 8a and b**. Figure 8a shows the CV curves of the samples at a scan rate of  $50 \text{ mV s}^{-1}$ . The area of the CV curve increased in the order of NPCN-14D, NPCN-11D, and PCN, respectively. Given that the surface area and pore volume of the NPCN samples were slightly lower than those of PCN, the increased area of the CV curve could be attributed to the faradic current derived from the nitrogen-containing functional groups in the NPCN samples. This is supported by that NPCN-14D, which had a higher nitrogen content, showed a wider CV area than NPCN-11D. To compare the rate capability, the specific capacitances of the samples at different current densities were calculated based on the discharging time (**Figure 8b**). NPCN-14D has achieved the highest a specific capacitance of  $350 \text{ F g}^{-1}$  at a current density of  $1 \text{ A g}^{-1}$ , which were higher than that of NPCN-11D ( $323 \text{ F g}^{-1}$ ) and PCN ( $279 \text{ F g}^{-1}$ ). NPCN-14D retained a capacitance of  $260 \text{ F g}^{-1}$  at a high current density of  $10 \text{ A g}^{-1}$ , with a rate performance of 74 %, which was higher than

those of NPCN-11D (212 F g<sup>-1</sup>, 70 %) and PC (181 F g<sup>-1</sup>, 65 %). **Figure 8c** shows the CV curves of NPCN-14D within the voltage range from -1.0 to 0 V<sub>Hg/HgO</sub> at different scan rates within 10 – 1000 mV s<sup>-1</sup>. The CV curve at a scan rate of 10 mV s<sup>-1</sup> exhibited a slightly deformed rectangle with a hump at a lower potential, indicating the faradic current that derived from N- and O-containing functional groups in NPCN-14D, which is consistent with the XPS and EA results. The CV curves at higher scan rates demonstrated a rectangular shape, which indicated that NPCN-14D had a high rate capability. The GCD curves at various current densities exhibited a similar trend to that of the CV curves (**Figure 8d**). Even at high current densities, there was no IR drop, which is related to internal resistance; this suggested that NPCN-14D had excellent capacitive properties.

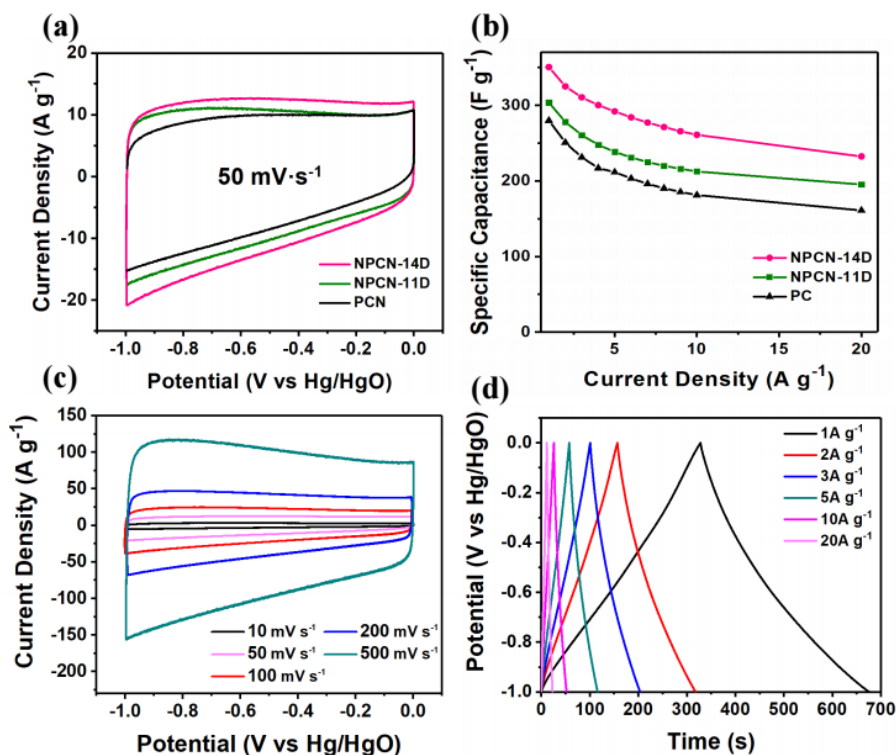


**Figure 8.** Electrochemical performances of PNC and NPCNs in the three-electrode system with 6M KOH electrolyte. a) CV curves at a scan rate of  $50 \text{ mV s}^{-1}$ , b) Specific capacitances at various current densities from 1 to  $20 \text{ A g}^{-1}$  of PCN, NPCN-11D, and NPCN-14D. c) CV curves at various scan rates from 10 to  $500 \text{ mV s}^{-1}$ , d) GCD curves at various current densities from 1 to  $20 \text{ A g}^{-1}$  of NPCN-14D.



To maximize the capacitive performance of NPCN-14D in practical cell applications, a symmetric supercapacitor using NPCN-14D as electrode material in a redox-mediated electrolyte was assembled. The indole-based macromolecule containing 5,6-dihydroxyindole/5,6-quinoneindole motifs for the redox additives in an aqueous electrolyte (IME) was synthesized through CV scanning at the rate of  $1000 \text{ mV s}^{-1}$ . The color of the dopamine solution transformed from transparent into brown after 24h. The change of the molecular size could be confirmed by DLS measurement (**Figure 9**). The size of the molecules was measured 100-250 nm after the electrochemical polymerization, which consistent with the previously reported results [29].

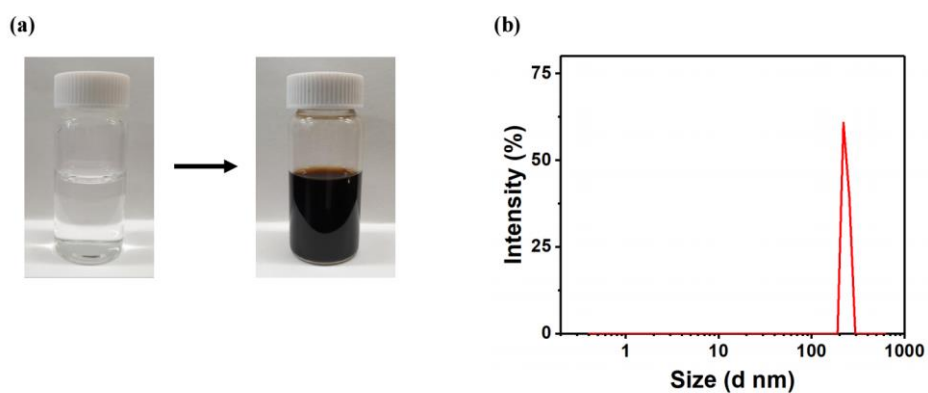


**Figure 9.** a) A color change of the dopamine solution resulting from the electrochemical polymerization and b) DLS measurement of IME.

The assembled symmetric supercapacitors were evaluated via several electrochemical tests. **Figure 10a** shows the CV curve of the fabricated cell at various scan rates ranging from  $25 \text{ mV s}^{-1}$  to  $1000 \text{ mV s}^{-1}$  with a potential window of  $0 - 1.2 \text{ V}$ . The curves at a relatively low scan rate displayed anodic and cathodic humps that were attributed to redox reactions. Notably, the rectangular shape was retained even at the high scan rate of  $1000 \text{ mV s}^{-1}$ , which indicated that the cell had a good rate performance. The GCD curves at different current densities had a deformed triangular shape, which was related to the redox reaction and corroborated the CV results (**Figure 10b**). **Figure 10c** shows the rate performance of the fabricated cell in IME and  $0.5\text{M H}_2\text{SO}_4$ . The electrode exhibited a capacitance of  $468 \text{ F g}^{-1}$  at a current density of  $1 \text{ A g}^{-1}$ . This value was relatively high compared to that in  $0.5\text{M H}_2\text{SO}_4$  ( $266 \text{ F g}^{-1}$ ), which appears to be due to the redox reaction of the additive in the electrolyte. Interestingly, the electrode retained a capacitance of  $233 \text{ F g}^{-1}$  at a relatively high current density of  $20 \text{ A g}^{-1}$  indicating that the macromolecules in the electrolyte caused a redox reaction even at very high current densities due to the small HLG. **Figure 10d** exhibits the Nyquist plot obtained via EIS in the assembled cell. In the Nyquist plot, the intersection between a high frequency line and  $Z'$  axis is related to

electrolyte resistance and the size of the semicircle in the middle-frequency area indicates the charge-transfer resistance of the cell. It can be seen that both of the electrolyte resistance and the charge-transfer resistance of the cell with IME is lower than these with 0.5 M H<sub>2</sub>SO<sub>4</sub>, which could be explained by the low HLG of IME. The polymerization of dopamine resulted in lower HLG of the molecules and the decreased HLG facilitated the electron transfer to acceptor, which increased ionic conductivity and allowed fast electron transfer within the molecules.

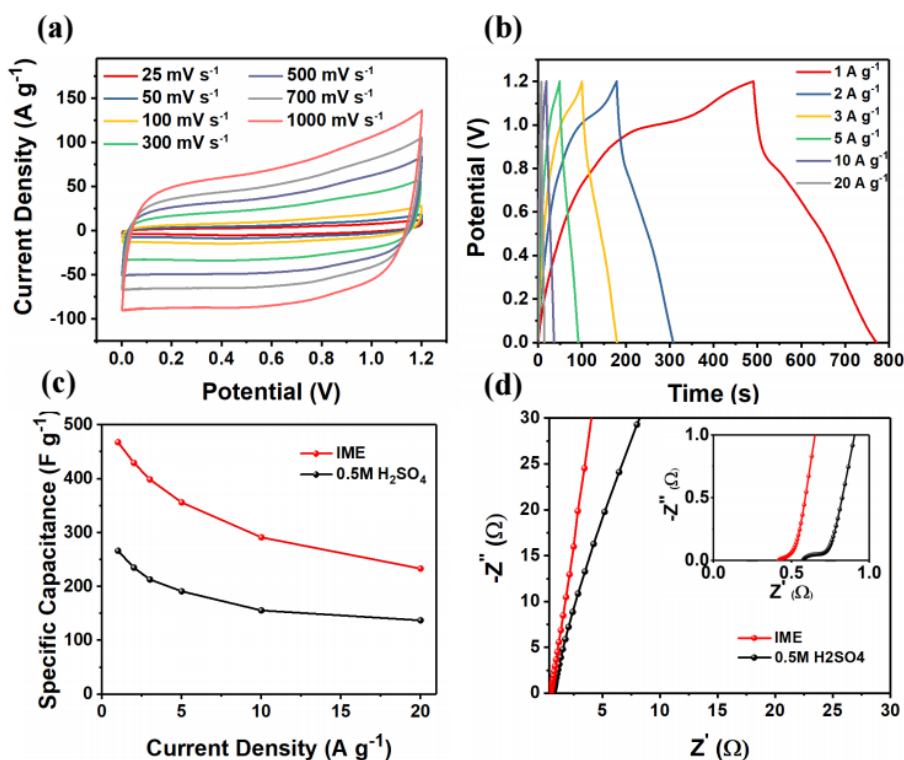


**Figure 10.** Electrochemical performances of NPCN-14D in the symmetric supercapacitors with indole based macromolecule electrolyte. a) CV curves at various scan rates from 25 to 1000 mV s<sup>-1</sup>. b) GCD curves and c) Specific capacitances at various current densities from 5 to 100 A g<sup>-1</sup>. d) Nyquist plot.

To confirm the stability of the assembled cell, a cycle test was conducted at a current density of  $20 \text{ A g}^{-1}$  (**Figure 11a**). The assembled cells maintained  $\sim 80 \%$  of their initial capacity after 3,000 cycles, indicating that the cells and redox electrolytes remained stable after repeated reactions at relatively high current densities. **Figure 11b** shows the energy-storage capacity and power performance of the cells in terms of energy and power densities. The assembled cell was able to store the energy density of  $1087 \text{ mWh kg}^{-1}$  at a power density of  $13.94 \text{ mW kg}^{-1}$  and  $371 \text{ Wh kg}^{-1}$  at the high power density of  $1395 \text{ W kg}^{-1}$ .

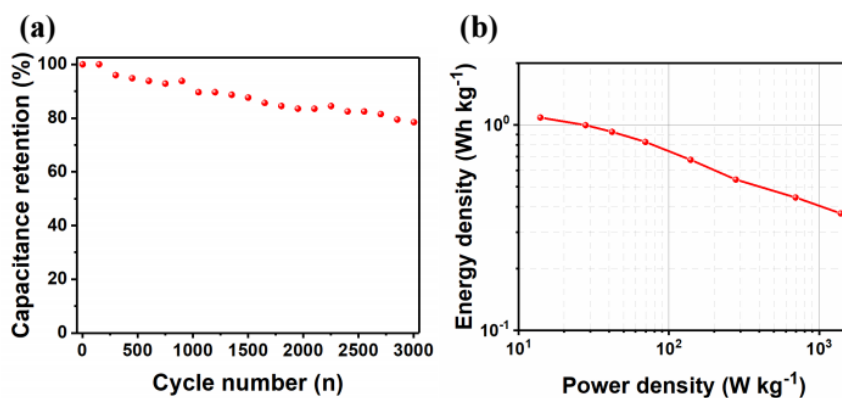


**Figure 11.** a) Cycle performance at 20 A g<sup>-1</sup>. b) Ragone plots of the symmetric supercapacitor.

## 4. Conclusions

In summary, N-doped interconnected porous carbon nanosheets derived from potassium citrate was prepared using post-heat-treatment with melamine. To induce melamine condensation during heat-treatment in the synthesis of NPCN, dwell time was set at the temperature of the condensation. The condensation of melamine was confirmed via FT-IR. As a result, the nitrogen-doping rate of the carbon synthesized with dwell time was around two time compared with that of the carbon without dwell time. The synthesized N-doped carbon showed an SSA of 1041.4  $\text{m}^2 \text{g}^{-1}$  and a total pore volume of 0.63  $\text{cm}^3 \text{g}^{-1}$  while maintaining the interconnected nanosheets structure. The NPCN-14D showed a specific capacitance of 350  $\text{F g}^{-1}$  at a current density of 1  $\text{A g}^{-1}$  in the three-electrode system. Moreover, the NPCN-14D was used as a symmetric supercapacitor paired with an indole-based macromolecule electrolyte, and it showed a specific capacitance of 468  $\text{F g}^{-1}$  at a current density of 1  $\text{A g}^{-1}$  and retain a specific capacitance of 233  $\text{F g}^{-1}$  at a relatively high current density of 20  $\text{A g}^{-1}$ .



## References

- [1] X. Zheng, J. Luo, W. Lv, D.W. Wang, Q.H. Yang, Two-Dimensional Porous Carbon: Synthesis and Ion-Transport Properties, *Adv Mater* 27 (2015) 5388-5395.
- [2] P. Simon, Y. Gogotsi, Materials for electrochemical capacitors, *Nat Mater* 7 (2008) 845-854.
- [3] R. Kotz, M. Carlen, Principles and applications of electrochemical capacitors, *Electrochimica Acta* 45 (2000) 2483-2498.
- [4] G. Wang, L. Zhang, J. Zhang, A review of electrode materials for electrochemical supercapacitors, *Chem Soc Rev* 41 (2012) 797-828.
- [5] L.L. Zhang, X.S. Zhao, Carbon-based materials as supercapacitor electrodes, *Chem Soc Rev* 38 (2009) 2520-2531.
- [6] X. Chen, R. Paul, L. Dai, Carbon-based supercapacitors for efficient energy storage, *National Science Review* 4 (2017) 453-489.
- [7] Z. Fan, J. Yan, L. Zhi, Q. Zhang, T. Wei, J. Feng, M. Zhang, W. Qian, F. Wei, A three-dimensional carbon nanotube/graphene sandwich and its application as electrode in supercapacitors, *Adv Mater* 22 (2010) 3723-3728.
- [8] Z. Fan, Y. Liu, J. Yan, G. Ning, Q. Wang, T. Wei, L. Zhi, F. Wei, Template-Directed Synthesis of Pillared-Porous Carbon Nanosheet

Architectures: High-Performance Electrode Materials for Supercapacitors, *Advanced Energy Materials* 2 (2012) 419-424.

[9] M.F. El-Kady, Y. Shao, R.B. Kaner, Graphene for batteries, supercapacitors and beyond, *Nature Reviews Materials* 1 (2016) 16033-16047.

[10] J. Wang, X. Yang, D. Wu, R. Fu, M.S. Dresselhaus, G. Dresselhaus, The porous structures of activated carbon aerogels and their effects on electrochemical performance, *Journal of Power Sources* 185 (2008) 589-594.

[11] H. Wang, Z. Xu, A. Kohandehghan, Z. Li, K. Cui, X. Tan, T.J. Stephenson, C.K. King'ondeu, C.M. Holt, B.C. Olsen, J.K. Tak, D. Harfield, A.O. Anyia, D. Mitlin, Interconnected carbon nanosheets derived from hemp for ultrafast supercapacitors with high energy, *Acs Nano* 7 (2013) 5131-5141.

[12] M. Sevilla, A.B. Fuertes, Direct Synthesis of Highly Porous Interconnected Carbon Nanosheets and Their Application as High-Performance Supercapacitors, *Acs Nano* 8 (2014) 5069-5078.

[13] X. Fan, C. Yu, J. Yang, Z. Ling, C. Hu, M. Zhang, J. Qiu, A Layered-Nanospace-Confinement Strategy for the Synthesis of Two-Dimensional Porous Carbon Nanosheets for High-Rate Performance Supercapacitors,

Advanced Energy Materials 5 (2015) 1401761-1401768.

[14] C. Chen, D. Yu, G. Zhao, B. Du, W. Tang, L. Sun, Y. Sun, F. Besenbacher, M. Yu, Three-dimensional scaffolding framework of porous carbon nanosheets derived from plant wastes for high-performance supercapacitors, Nano Energy 27 (2016) 377-389.

[15] K. Jurewicz, K. Babel, A. Żiółkowski, H. Wachowska, Ammoxidation of active carbons for improvement of supercapacitor characteristics, Electrochimica Acta 48 (2003) 1491-1498.

[16] G. Lota, B. Grzyb, H. Machnikowska, J. Machnikowski, E. Frackowiak, Effect of nitrogen in carbon electrode on the supercapacitor performance, Chemical Physics Letters 404 (2005) 53-58.

[17] K.N. Wood, R. O'Hayre, S. Pylypenko, Recent progress on nitrogen/carbon structures designed for use in energy and sustainability applications, Energy Environ. Sci. 7 (2014) 1212-1249.

[18] M. Inagaki, M. Toyoda, Y. Soneda, T. Morishita, Nitrogen-doped carbon materials, Carbon 132 (2018) 104-140.

[19] L. Hao, X. Li, L. Zhi, Carbonaceous electrode materials for supercapacitors, Adv Mater 25 (2013) 3899-904.

[20] Q. Liu, J. Zhong, Z. Sun, H. Mi, Cross-linked carbon networks constructed from N-doped nanosheets with enhanced performance for

supercapacitors, *Applied Surface Science* 396 (2017) 1326-1334.

[21] Y.-Y. Wang, B.-H. Hou, H.-Y. Lü, C.-L. Lü, X.-L. Wu Hierarchically Porous N-Doped Carbon Nanosheets Derived From Grapefruit Peels for High-Performance Supercapacitors, *ChemistrySelect* 1 (2016) 1441-1447.

[22] M. Chen, D. Yu, X. Zheng, X. Dong, Biomass based N-doped hierarchical porous carbon nanosheets for all-solid-state supercapacitors, *Journal of Energy Storage* 21 (2019) 105-112.

[23] D. Chen, S. Wang, Z. Zhang, H. Quan, Y. Wang, Y. Jiang, M.J. Hurlock, Q. Zhang, Molten NaCl-induced MOF-derived carbon-polyhedron decorated carbon-nanosheet with high defects and high N-doping for boosting the removal of carbamazepine from water, *Environmental Science: Nano* 7 (2020) 1205-1213.

[24] M. Rybin, A. Pereyaslavl'tsev, T. Vasilieva, V. Myasnikov, I. Sokolov, A. Pavlova, E. Obraztsova, A. Khomich, V. Ralchenko and E. Obraztsova, Efficient nitrogen doping of graphene by plasma treatment, *Carbon* 96 (2016) 196-202.

[25] R. Liu, Y. Wang, X. Wu, Two-dimensional nitrogen and oxygen Co-doping porous carbon nanosheets for high volumetric performance supercapacitors, *Microporous and Mesoporous Materials* 295 (2020)

109954-109961.

[26] Z.S. Wu, W.C. Ren, L. Xu, F. Li, H.M. Cheng, Doped Graphene Sheets As Anode Materials with Superhigh Rate and Large Capacity for Lithium Ion Batteries, *Acs Nano* 5 (2011) 5463-5471.

[27] L.S. Panchakarla, K.S. Subrahmanyam, S.K. Saha, A. Govindaraj, H.R. Krishnamurthy, U.V. Waghmare, C.N.R. Rao, Synthesis, Structure, and Properties of Boron- and Nitrogen-Doped Graphene, *Advanced Materials* 21 (2009) 4726-4730.

[28] S. Roldan, C. Blanco, M. Granda, R. Menendez, R. Santamaria, Towards a further generation of high-energy carbon-based capacitors by using redox-active electrolytes, *Angew Chem, Int. Ed.* 50 (2011) 1699-701.

[29] T. Xiong, W.S.V. Lee, L. Chen, T.L. Tan, X. Huang, J. Xue, Indole-based conjugated macromolecules as a redox-mediated electrolyte for an ultrahigh power supercapacitor, *Energy & Environmental Science* 10 (2017) 2441-2449.

[30] L. Yan, D. Li, T. Yan, G. Chen, L. Shi, Z. An, D. Zhang, Confining Redox Electrolytes in Functionalized Porous Carbon with Improved Energy Density for Supercapacitors, *ACS Appl Mater Interfaces* 10 (2018) 42494-42502.

- [31] K. Jayaramulu, D.P. Dubal, B. Nagar, V. Ranc, O. Tomanec, M. Petr, K.K.R. Datta, R. Zboril, P. Gomez-Romero, R.A. Fischer, Ultrathin Hierarchical Porous Carbon Nanosheets for High-Performance Supercapacitors and Redox Electrolyte Energy Storage, *Adv Mater* 30 (2018) 1705789-1705798.
- [32] S. Dyjak, W. Kiciński, A. Huczko, Thermite-driven melamine condensation to  $C_xN_yH_z$  graphitic ternary polymers: towards an instant, large-scale synthesis of g-C<sub>3</sub>N<sub>4</sub>, *Journal of Materials Chemistry A* 3 (2015) 9621-9631.
- [33] Y.C. Zhao, D.L. Yu, H.W. Zhou, Y.J. Tian, O. Yanagisawa, Turbostratic carbon nitride prepared by pyrolysis of melamine, *Journal of Materials Science* 40 (2005) 2645-2647.
- [34] B.V. Lotsch, W. Schnick, New light on an old story: formation of melam during thermal condensation of melamine, *Chemistry* 13 (2007) 4956-4968.
- [35] A. Sattler, S. Pagano, M. Zeuner, A. Zurawski, D. Gunzelmann, J. Senker, K. Muller-Buschbaum, W. Schnick, Melamine-melam adduct phases: investigating the thermal condensation of melamine, *Chemistry* 15 (2009) 13161-13170.
- [36] H.B. Zheng, W. Chen, H. Gao, Y.Y. Wang, H.Y. Guo, S.Q. Guo, Z.L.

- Tang, J.Y. Zhang, Melem: an efficient metal-free luminescent material, *J. Mater. Chem. C* 5 (2017) 10746-10753.
- [37] D.L. Yu, J.L. He, Z.Y. Liu, B. Xu, D.C. Li, Y.J. Tian, Phase transformation of melamine at high pressure and temperature, *Journal of Materials Science* 4 (2007) 689-695.
- [38] W. Kulisch, M.P. Delplancke-Ogletree, J. Bulii, M. Jelinek, K. Jurek, J. Zemek, J. Klimovic, Characterization of magnetron sputtered carbon nitride films, *Diamond and related materials* 8 (1999) 1039-1045.
- [39] M. Seredych, D. Hulicova-Jurcakova, G.Q. Lu, T.J. Bandoz, Surface functional groups of carbons and the effects of their chemical character, density and accessibility to ions on electrochemical performance, *Carbon* 46 (2008) 1475-1488.
- [40] N.A. Travlou, C. Ushay, M. Seredych, E. Rodríguez-Castellón, T.J. Bandoz, Nitrogen-Doped Activated Carbon-Based Ammonia Sensors: Effect of Specific Surface Functional Groups on Carbon Electronic Properties, *ACS Sensors* 1 (2016) 591-599.
- [41] M.S. Dresselhaus, A. Jorio, M. Hofmann, G. Dresselhaus, R. Saito, Perspectives on carbon nanotubes and graphene Raman spectroscopy, *Nano Lett* 10 (2010) 751-758.
- [42] A.C. Ferrari, J. Robertson, Interpretation of Raman spectra of

disordered and amorphous carbon, Phys Rev B 61 (2000) 14095-14107.



## 국 문 초 록

다공성 탄소 나노시트는 제작이 간단하며 효율적인 구조를 통해 전해질 이온의 빠른 이동을 가능케 한다는 점에서 전기 이중층 커패시터 전극물질로 많은 주목을 받고 있다. 그렇지만 정전기적 흡착으로 전하를 저장하는 탄소 물질의 특성으로 전극물질로 활용 시 상대적으로 낮은 커패시턴스를 보인다는 점이 지적받고 있다. 본 연구에서는 다공성 탄소 나노시트에 효과적인 열처리 방법을 통해 질소를 도핑함으로써 용량을 향상시켰고, 합성된 탄소 물질을 산화/환원반응 첨가제가 들어간 전해질에 접목시켜 추가적인 성능 향상을 꾀하였다.

먼저, 포타슘 사이트레이트를 열분해하여 다공성 탄소 나노시트가 상호 연결된 형태의 탄소 물질을 합성하였다. 합성된 탄소 물질에 질소 도핑을 하기 위해 질소 함유량이 풍부한 멜라민을 탄소 물질과 교반하여 열처리하였는데, 열처리 과정 중 특정 온도에서 머무는 시간을 설정함으로써 멜라민의 중합을 유도하였다. 열처리 과정 중 발생한 중합은 멜라민의 손실을 최소화하였고, 그 결과 최종 질소 도핑 비율은 2배 가량 향상되었다. 질소 도핑된 탄소 물질의 전기화학적 특성을 3전극 상황에서 확인해 본 결과,  $1 \text{ A g}^{-1}$ 에서 도핑되지 않은 탄소 물질 대비 25 % 증가한  $360 \text{ F g}^{-1}$ 의 용량을 보였다. 또한, 대칭 2전극 상황에서는 산화/환원 첨가제가 들어간

전해질과 접목되어  $1 \text{ A g}^{-1}$ 에서  $468 \text{ F g}^{-1}$ 의 더욱 향상된 용량을 발현하였다.

본 연구는 다공성 탄소 나노시트에 질소 도핑을 하기 위해 멜라민의 중합반응을 활용한 효율적인 방법을 제시했다는 점과, 질소 도핑 및 산화/환원 첨가제가 들어간 전해질을 활용해서 다공성 탄소 나노시트의 커패시턴스 향상을 이뤄냈다는 점에서 의의가 있다.

**주요어:** 슈퍼커패시터, 상호 연결된 다공성 탄소 나노시트, 질소 도핑, 멜라민 중합, 산화/환원 첨가제가 포함된 수용액 전해질

학 번: 2018-24374